On the mechanism of carbon dioxide corrosion of mild steel: Experimental investigation and mathematical modeling at elevated pressures and non-ideal solutions

Aria Kahyarian*, Srdjan Nesic

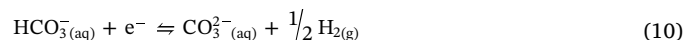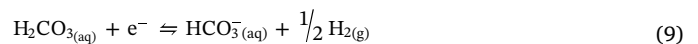*Institute for Corrosion and Multi-phase Flow Technology, Ohio University, Athens, OH, USA*

ABSTRACT

The mechanistic study of uniform CO_2 corrosion in the pH range from 4 to 6 and CO_2 partial pressures up to 15 bar showed that neither H_2CO_3 nor HCO_3^- were reduced directly during the corrosion process to any appreciable extent. The significant effect of these carbonate species on the corrosion process is through their homogeneous dissociation insider the boundary layer. This mechanistic view was further quantitatively verified using a comprehensive mathematical model, developed with hydrogen ion reduction as the sole cathodic reaction while accounting for the effect of homogeneous chemical reactions, turbulent flow mixing, and non-ideal solution properties.

1. Background

The mechanism of carbon dioxide (CO_2) corrosion of mild steel has been a controversial subject for decades, perhaps due to the complexities arising from the presence of numerous chemically and (what was assumed) electrochemically active species in an aqueous acidic CO_2/ H_2O system. In the conventional understanding, CO_2 corrosion is a result of a series of chemical reactions (Reactions (1)–(5)) and electrochemical reactions (Reactions (6)–(10)). The chemical reactions are associated with the CO_2/H_2O equilibria in acidic solutions. The complexity of this chemical system alone has made it the subject of numerous studies over many decades [1–8]. Upon dissolution in water (Reaction (1)), the dissolved CO_2 undergoes a series of chemical reactions, starting with the hydration reaction to produce carbonic acid (H_2CO_3). Carbonic acid, as a diprotic weak acid, is partially dissociated to form hydrogen (H^+) and bicarbonate (HCO_3^-) ions, which further dissociates to hydrogen ion and carbonate ion (CO_3^{2-}), as shown by Reactions (3) and (4). Water, present as the solvent, can also dissociate according to Reaction (5).

$$CO_{2(g)} \leftrightarrows CO_{2(aq)} \tag{1}$$

$$CO_{2(aq)} + H_2O_{(l)} \leftrightarrows H_2CO_{3(aq)} \tag{2}$$

$$H_2CO_{3(aq)} \leftrightarrows HCO_{3(aq)}^- + H^+_{(aq)} \tag{3}$$

$$HCO_{3(aq)}^- \leftrightarrows CO_{3(aq)}^{2-} + H^+_{(aq)} \tag{4}$$

$$H_2O_{(l)} \leftrightarrows OH^-_{(aq)} + H^+_{(aq)} \tag{5}$$

It was commonly believed that the electrochemistry of CO_2 corrosion is an equally complicated system. While iron dissolution (oxidation partial of Reaction (6)) is the main anodic reaction, the cathodic reactions (reduction partials of Reactions (7)–(10)) include the H^+ reduction as well as the direct reduction of other weak acids present in the system, e.g. H_2CO_3, HCO_3^- and H_2O.

$$Fe^{2+}_{(aq)} + 2e^- \leftrightarrows Fe_{(s)} \tag{6}$$

$$H^+_{(aq)} + e^- \leftrightarrows \frac{1}{2}H_{2(g)} \tag{7}$$

$$H_2O_{(l)} + e^- \leftrightarrows OH^-_{(aq)} + \frac{1}{2}H_{2(g)} \tag{8}$$

$$H_2CO_{3(aq)} + e^- \leftrightarrows HCO_{3(aq)}^- + \frac{1}{2}H_{2(g)} \tag{9}$$

$$HCO_{3(aq)}^- + e^- \leftrightarrows CO_{3(aq)}^{2-} + \frac{1}{2}H_{2(g)} \tag{10}$$

This classic mechanistic view has evolved gradually from the 1970s to the early 2000s. Some of the landmark studies are briefly reviewed in the following, while a more comprehensive historical review of the subject can be found elsewhere [9–11]. The earliest reports suggesting a significant role for H_2CO_3 in CO_2 corrosion are those published by de Waard and Milliams [12,13]. The authors argued that in CO_2-saturated

acidic solutions the direct reduction of H_2CO_3 is the dominant cathodic reaction, and ignored other possible cathodic reactions including H^+ reduction. The mechanism of cathodic reactions as suggested in that study consists of the direct reduction of H_2CO_3, followed by the association reaction of HCO_3^- with H^+. While we now know that the proposed mechanism by de Waard and Milliams [12,13] was a major over-simplification, it is easy to trace how development of the mechanistic understanding of CO_2 corrosion initiated with that seminal study.

The significance of the chemical reactions in CO_2/H_2O system, in particular the role of CO_2 hydration reaction in defining the cathodic limiting currents, was first recognized by Schmitt and Rothmann [14]. Considering the low equilibrium constant of the hydration reaction, only a small fraction of dissolved CO_2 reacts to form H_2CO_3. Therefore, there is a large reservoir of dissolved CO_2 available in the boundary layer, that can replenish the concentration of H_2CO_3 through the hydration reaction as it is consumed in the corrosion process. In fact, this reaction is now known as a unique characteristic of CO_2 corrosion that differentiates it not only from corrosion in strong acid solutions but also from the corrosion in the presence of other weak acids such as carboxylic acids and hydrogen sulfide.

CO_2 corrosion as a complex but systematic interaction of chemical, electrochemical, and mass transfer processes was first recognized in the studies by Gray et al. [15,16]. Gray et al. used a mechanistic approach to represent the reduction of H^+ as well as the direct reduction of H_2CO_3 and HCO_3^-, while incorporating the effect of mass transfer and CO_2 hydration reaction occurring in the boundary layer. What can be considered as the first (elementary) mechanistic model for analysis of polarization data and corrosion rates in CO_2 saturated solutions [11].

The final development in the classic mechanistic view of CO_2 corrosion, is the result of the introduction of more comprehensive mathematical models in the late 1990s and 2000s [17–20]. These models allowed the chemical and electrochemical aspects of CO_2 corrosion to be coupled properly. It was only after this step that the significance of the homogeneous dissociation reactions (Reactions (3) and (4)) in the boundary layer were understood.

The introduction of the comprehensive mathematical models also paved the way to what it can be called the *modern mechanistic view to CO_2 corrosion*. The quantitative analysis in these studies allowed the observation of the (now well-understood) fact that the limiting currents in CO_2-saturated solutions can be properly quantified without considering the direct reduction of H_2CO_3 [17–20]. That is via a parallel reaction pathway to direct reduction of H_2CO_3 through homogeneous dissociation of H_2CO_3 (Reactions (3)), followed by the reduction of H^+ at the metal surface. Considering that at the limiting current conditions the increasing surface pH shifts the chemical equilibrium towards the dissociation reaction, this parallel reaction sequence can be dominating depending on reaction kinetics. This observation is of great significance as it questions the basis of the classical mechanistic view of CO_2 corrosion developed in earlier studies. For example, in the study by Gray et al. [15,16] (and other similar models developed over the years [21–24]), the mathematical model used to evaluate the reaction mechanism does not account for the dissociation reactions inside the boundary layer, as described elsewhere [9,11]. Therefore, the limiting currents could only be explained if H_2CO_3 (and HCO_3^-) was considered to be directly reduced at the metal surface. However, considering the possibility of the parallel reaction pathway through the dissociation reaction, the previous mechanistic arguments now appear to lack sufficient evidence in their support. The latter mechanistic view suggests that the limiting currents may behave similarly irrespective of whether the weak acid is directly reduced or not, hence, the electrochemical activity of H_2CO_3 needs to be re-evaluated by focusing on the behavior of the charge transfer controlled cathodic currents. It can be hypothesized that, at a fixed pH where the rate of H^+ reduction is constant, if the H_2CO_3 is electrochemically active the charge transfer controlled current would increase in response to an increase in its concentration

(higher pCO_2). Conversely, if H_2CO_3 is not significantly electroactive, the charge transfer controlled currents would not be affected by the concentration of this species.

At the same time, other studies focused on the electrochemical activity of carboxylic acids in mild steel corrosion, were going through similar mechanistic discussions [25–30]. Similarly to the case of H_2CO_3 reduction, acetic acid was also conventionally assumed to be directly reduced in the corrosion process. However, in more recent studies there is a consensus that the direct reduction of acetic acid is insignificant and its main contribution is through homogeneous dissociation inside the boundary layer that buffers the surface concentration of H^+ [25–28]. The similarity between the case of acetic acid and the case of H_2CO_3 further indicates the need for a more in-depth mechanistic investigation of CO_2 corrosion mechanisms.

The discussion on the significance of H_2CO_3 reduction in CO_2 corrosion can be traced back to the study by Linter and Burstein [31]. However, the subject gained more attention only in more recent years [32–35]. A detailed review of the earlier studies, the validity of the experimental conditions and corresponding mechanistic arguments, as well as the persisting knowledge gap can be found in the previous publications [9–11,34,35]. Our earlier studies [35–38] were aimed to address such persisting deficiencies in the mechanistic arguments on the significance of H_2CO_3 reduction. The experiments in these studies were performed using a thin channel flow cell at high flow velocities and CO_2 partial pressures up to 5 bar and pH values up to 5. The reported experimental data, particularly those obtained at 10 °C, showed the charge transfer controlled currents in an extended range of potentials on X65 mild steel. This range of current densities was found to remain unaffected by pCO_2 ranging from 0 to 5 bar at pH values up to 5, hence, the direct reduction of H_2CO_3 was shown to be insignificant on mild steel surface in that range. This mechanism was incorporated in a comprehensive mathematical model in order to provide further quantitative evidence for this mechanistic view [35]. The agreement of the results from the model, both in the cathodic charge transfer controlled range and in the limiting current range, was considered as further evidence that the direct reduction of H_2CO_3 is not significant in CO_2 corrosion of mild steel. As expected, the presence of H_2CO_3 only increased the magnitude of the limiting current as a result of homogeneous H_2CO_3 dissociation and CO_2 hydration in the vicinity of the metal surface. The reported experimental corrosion rates as a function of pCO_2 were found to agree well with those calculated by using a model based on this mechanistic view [35]. It was shown that when the cathodic currents are under charge transfer control, increasing the partial pressure of CO_2 has no significant effect on corrosion rates, whereas, when the corrosion rates were under the influence of the limiting current, increasing the pCO_2 increased the corrosion rates almost linearly.

It is important to realize that the significance of the electrochemical activity of H_2CO_3 or any other weak acid is always relative to that of H^+ reduction. Since the latter reaction is always occurring in acidic solutions, it cannot be stated with absolute certainty that H_2CO_3 (or for that matter any other weak acids) is not electrochemically active in all conditions. The word "insignificant" – that used here to describe the electrochemical activity of H_2CO_3 – is as compared to the rate of H^+ reduction and it is always bound to the conditions of a particular study. As a relative measure, the ratio of H_2CO_3 to H^+ concentrations can be used to quantify the validity range of such mechanistic conclusions. The case of direct reduction of H_2CO_3 has been studied previously [32–36,39,40], for the particular case of mild steel surface the existing data in the literature covers $[H_2CO_3]/[H^+]$ ratio of up to about 30 in some recent studies [34,35,37]. However, the industrial application could commonly encounter conditions with significantly larger values, especially at higher pH values with elevated CO_2 partial pressures e.g. at pH 6 even at 1 bar CO_2 the $[H_2CO_3]/[H^+]$ ratio is about 50. Therefore, there is a need to prove the validity of such a mechanistic argument over an extended range of conditions, so that it can be used
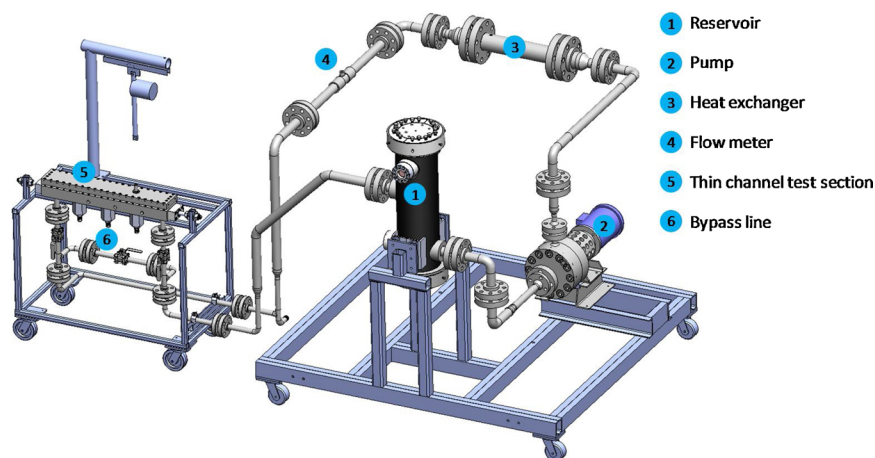
Fig. 1. Schematics of the high-pressure thin channel flow cell.

with reasonable certainty to describe the corrosion process in a broad range of conditions seen in various applications.

The role of bicarbonate ion is another key aspect of CO_2 corrosion of mild steel. The classic mechanistic view of CO_2 corrosion assumes that HCO_3^- is also electrochemically active and can be directly reduced during the corrosion process via reaction (10) [10,11,16,22,41,42]. This reaction was believed to be significant in the near neutral and mildly alkaline pH range. Considering the recent developments in mechanistic understandings of CO_2 corrosion, the significance of HCO_3^- reduction can also be questioned. Similar to the case of H_2CO_3, arguments on the ability of HCO_3^- to buffer the H^+ concentration can be presented. Nonetheless, the experimental and quantitative analysis of the mechanism of HCO_3- contribution to cathodic current is an open subject, which we attempt to address in the present study.

The present investigation expands on previous studies [35–38] both in terms of the range of the experimental conditions and mathematical modeling of CO_2 corrosion of mild steel. In the present study, the experiments were conducted in a high-pressure thin channel flow cell in order to allow for relatively high pCO_2 and high flow velocities. The conditions cover the pCO_2 range from 1 to 15 bar, velocities up to 4.4 m/s, and the pH range 4–6. That range of parameters can be considered a reasonable representative of a great majority of the corrosion conditions as seen in the oil and gas transmission pipelines, and it covers the $[H_2CO_3]/[H^+]$ ratio of up to about 700. The experiments at higher pH and pCO_2 also provides an opportunity to investigate the effect and the mechanism of HCO_3^- contribution to cathodic currents.

The comprehensive mathematical models can be seen as accurate corrosion rate predictive tools [9,11,27,35], and effective means for mechanistic analysis of the experimental data as well as quantitative evaluation of the physicochemical constants. The discussion of the electrochemical activity of weak acids (including H_2CO_3 and HCO_3^-) do not impose any technical difficulties on comprehensive mathematical models. The same modeling approach can be used to simulate the polarization behavior and corrosion rates, with the difference being in the electrochemical reactions assumed at the metal surface boundary. Nonetheless, the relevant physicochemical parameters needs to be re-evaluated to be consistent with the incorporated mechanistic view [27,35].

As compared to the models developed previously based on the direct H_2CO_3 and HCO_3^- reduction reaction [9,11,19,43,44], both of which are now shown to be insignificant as discussed in the following sections, the accuracy of the models based on buffering effect mechanism is directly tied to the accuracy of the kinetic and thermodynamic representation of the homogeneous chemical reactions. As it is shown in a recent study [40], the polarization response of a system with "buffering effect" as the governing mechanism (no direct weak acid reduction) is dramatically influence by the kinetics and thermodynamics of the weak

acid dissociation reaction. Therefore, the accuracy of the predicted corrosion rates and polarization curves are critically tied to accuracy of the rate of chemical reactions at the bulk and inside the boundary layer. In particular, when attempting to discuss CO_2 corrosion or predict its rate in near neutral pH values (e.g. pH 6) specially at elevated pCO_2, the high concentration of dissolved ionic species leads to a significant departure of the activity coefficients from unity, hence, the ideal solution assumption used in previous models [19,35,45,46] is no longer valid. The solution non-idealities affect almost all aspects of corrosion, including mass transfer and charge transfer processes as well as the kinetics and the thermodynamics of the homogeneous chemical reactions. In that case, the model needs to incorporate the effect of non-ideal solution properties to reasonably and accurately represent the system.

In the present study, the water chemistry calculation and the kinetic rate constants of the chemical reactions associated with H_2O/CO_2 system is reviewed in detail to address such concerns. When necessary the physicochemical parameters were obtained based on the experimental data and the existing literature. The mathematical model in the present study is also extended to cover the moderately concentrated solutions range to represent the non-idealities of the system. The water chemistry calculations, as it concerns CO_2 corrosion, are framed in term of activities of the species using Pitzer's specific interaction model. Furthermore, the electrochemical model was coupled with a Pitzer's model in order to incorporate the effect of variable non-idealities inside the boundary layer into the transfer processes as well as the homogeneous chemical reaction and ultimately corrosion rate calculations.

2. Methodology

2.1. Experimental procedures

The experiments were carried out in the high-pressure thin channel flow cell (HPTCFC) as depicted in Fig. 1. All the components of the HPTCFC test apparatus are made of 316 L stainless steel. The experimental setup consists of a mixing tank, also used for pH measurement and pH adjustment, a heat exchanger used for temperature control, a high-pressure pump, and the test section. The heat exchanger was connected to an industrial chiller (AIR 3000 from Coolant Chillers Inc.) in order to remove the heat generated by the pump and allow the experiments to be conducted below room temperature. The temperature was monitored using thermocouples placed inside the tank and the test section. The test section (thin channel flow cell) with 76 cm flow length, had a single-phase fluid flow through a 4.78 mm high, and 63.5 mm wide channel. The pump (Leeson G131510.00 series with 7.5 hp) output was adjusted to provide the required flow velocity, which was measured using a turbine flow meter (Omega FTB-1308).

The typical experimental procedure started with filling the test

apparatus with 50 L deionized water, followed by addition of 292 g of NaCl, to make 0.1 M NaCl solution. The solution was then deoxygenated using pure CO_2 gas flowed through a sparger installed at the interior bottom of the tank. In order to ensure proper deoxygenation, the gas outflow was monitored using an oxygen sensor (Orbisphere). The maximum dissolved oxygen concentration at the end of the deoxygenation step was 2 ppb_m throughout all experiments, achieved typically after about 2 h of continuous purging. In the experiments at elevated pressures, after the deoxygenation step, the output gas flow was shut off and the system was pressurized to the targeted value. The pressure was monitored with a digital pressure gauge (Honeywell FPG1Dl) with ± 0.1% accuracy. As a criterion that the system has reached chemical equilibrium, constant pressure and pH readout over 30 min was used (usually achieved after about 4 h). The pH of the solution was measured using a high-pressure glass pH probe (Corr Instruments, Inc.). This procedure was followed by pH adjustment to the target value by gradually injecting a deoxygenated, concentrated NaOH solution into the tank. In a few cases where a large quantity of sodium ions was required to achieve the targeted pH (e.g. 15 bar CO_2 at pH 6) the required amount of sodium was pre-calculated and added into the solution in the form of sodium bicarbonate powder before the deoxygenation step. All the chemicals used in the present study were research grade (Fisher Scientific).

The test section in the present study allowed a three electrode arrangement with an in-house built Ag/AgCl reference electrode mounted into the cell lid across from the working electrode, as shown in Fig. 2, and the channel body serving as the counter electrode. The working electrodes were made of either API 5L X65 mild steel or 316L stainless steel with the chemical composition shown in Table 1. The working electrode assembly was made from a 316L stainless steel casing, with the disk-shaped working electrode at the center. The working electrode was isolated from the structure and the casing using an epoxy resin (LOCTITE Stycast 2850FT). Prior to each measurement, the electrode was abraded using 600 grit silicon carbide paper, rinsed and sonicated in isopropanol alcohol, and dried using nitrogen gas. The electrode was then flush mounted to the bottom of the test section just before initiating the electrochemical measurement. The test section was immediately purged with CO_2 gas and pressurized to the same level as the tank. The solution, prepared by the procedure described above, was then introduced into the test section. The experimental conditions of the present study are summarized in Table 2.

The electrochemical measurements for the API 5L X65 mild steel electrode were done using a Gamry Reference 600 potentiostat in the following order: (a) 15 min monitoring of the open circuit potential (OCP), (b) linear polarization resistance (LPR) measurement, (c) 5 min at OCP, (d) potentiodynamic measurement, (e) 5 min at OCP, (f) electrochemical impedance spectroscopy (EIS) measurement. The OCP measurements reached a steady potential within the first 15 min. The LPR measurements were done using 0.125 mV s^{-1} scan rate and 1 s^{-1}

sampling period at the potential range from −5 mV to +5 mV vs. OCP. No significant change in OCP was observed after LPR measurements. The steady state potentiodynamic measurements were done using staircase voltammetry with a scan rate of 0.5 mV s^{-1} and sampling period of 2 s^{-1}. The cathodic and anodic polarization curves were obtained in separate experiments by scanning the potential from OCP towards more negative and more positive potentials, respectively. The EIS measurements, used to obtain the solution resistance, were conducted at OCP with 5 mV AC voltage perturbation, at the frequency range of 10 kHz to 0.2 Hz and 10 points/decade.

For the experiments on 316 L stainless steel, in order to avoid the complications associated with evolution of a passive layer, the initial OCP monitoring was minimized to 2 min. That step was followed by the potentiodynamic measurement, 5 min at OCP, and the EIS measurement. The other electrochemical measurement parameters were identical to those used for the X65 mild steel surface. A good reproducibility of the potentiodynamic measurements and the absence of any unexplained variations in the obtained polarization curves, was taken as confirmation that the effects of any evolution of the passive layer was circumvented.

2.2. The mathematical model

2.2.1. Water chemistry calculation

As the first step in any quantitative discussion of the polarization curves and corrosion rate data, the solution speciation must be obtained. That is essential to determine the concentration of the chemical species, in order to establish their chemical and electrochemical contributions to the overall corrosion process. The reactions associated with the chemical equilibria of a H_2O/CO_2 system in an acidic solution were shown above by Reactions (1) through (4). The solution speciation can be obtained by finding the concentrations that satisfy all the equilibrium expressions associated with these homogeneous chemical reactions.

Carbon dioxide dissolution equilibrium, Reaction (1), can be quantified in terms of a modified Henry's law based on the Kriechevsky–Kasarnovsky treatment [47], which has been frequently used to assess CO_2 solubility in water [6,48,49]:

$$\frac{f_{CO_2}}{a_{CO_2}} = H_{CO_2} e^{\left(\int_{P_{ws}}^{P} \frac{\overline{V}_{m,CO_2}}{RT} dP\right)} \tag{11}$$

where on the left hand side, the numerator is the fugacity of CO_2 (bar) in the gas phase ($f_{CO_2} = p_{CO_2} \varphi_{CO_2}$), and p_{CO_2} is the partial pressure of CO_2 (bar), while the denominator is the activity of CO_2 in the solution ($a_{CO_2} = m_{CO_2} \gamma_{CO_2}$), and m is the molal concentration of CO_2. It should be noted that the water chemistry calculations in CO_2/H_2O systems have been conventionally done using *molal* concentration basis, which is followed here as well. In order to couple these calculations with the electrochemical model that is conventionally developed by using the
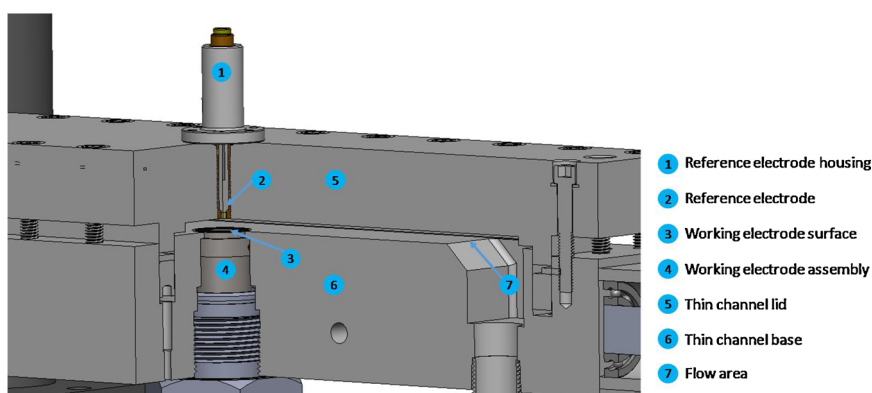

Fig. 2. The schematics of the thin channel test section and electrode arrangement.

Table 1
Chemical composition of working electrodes in wt.%.

	S	Cu	P	V	C	Cr	Mo	Si	Ni	Mn	Co	Fe
X65	0.009	–	0.009	0.047	0.13	0.14	0.16	0.26	0.36	1.16	–	Balance
SS 316L *	0.025	0.59	0.035	0.05	0.018	16.65	2.04	0.54	10.12	1.51	0.33	Balance

* Other elements with less than 0.1 wt.% concentrations: titanium, tin, tantalum, columbium, aluminum, boron, vanadium.

Table 2
Experimental conditions.

Test apparatus	Thin channel flow, three electrode arrangement
Flow velocity	1.8 m s^{-1} to 5.5 m s^{-1}
Materials	API X65 5L Mild steel
	316L stainless steel
Temperature	$10\,^{\circ}\text{C}$ to $40\,^{\circ}\text{C}$ ($\pm\ 0.5$)
pH	3.0–6.0 ($\pm\ 0.02$)
pCO$_2$	0 to 15 bar ($\pm\ 0.1\%$)
Supporting electrolyte	0.1 M NaCl

molar based concentrations, unit conversion needs to be employed.

On the right hand side of Equation (11), H_{CO_2} is the Henry's constant determined at saturation pressure of water, as shown below in Equation (14), and the exponential term in Equation (11) is the so-called Poynting pressure correction factor that essentially accounts for the change of Henry's constant with pressure. The integral domain in Equation (11) is from water saturation pressure (P_{ws} in Table 3) to the total pressure of the system (in bar), suggesting that this parameter is significant only at very high pressures. The partial molar volume of CO_2 in the aqueous phase, $\overline{V}_{m,CO_2}$ in m^3/mol, appearing in Equation (11) was determined by Garcia et al. [50] and it is reworked to be expressed in terms of Kelvin temperature as shown in Table 3. For a binary H$_2$O/CO$_2$ system, carbon dioxide partial pressure is $P_{CO_2} = P_{tot} - P_{ws}$, with P_{tot} being the total pressure of the system and P_{ws} being the saturation pressure of water (bar).

In the literature on the equilibrium and speciation of the CO$_2$/H$_2$O system, it is customary to lump the concentration of the dissolved CO$_2$ with H$_2$CO$_3$ to define $C_{CO_{2(aq)}^*} = C_{CO_{2(aq)}} + C_{H_2CO_{3(aq)}}$. Therefore, the equilibria are discussed in terms of Reaction (12) and Reaction (13), where H$_2$CO$_3$ is not explicitly considered.

$$CO_{2(g)} \rightleftharpoons CO_{2(aq)}^* \tag{12}$$

$$CO_{2(aq)}^* + H_2O_{(l)} \rightleftharpoons HCO_{3(aq)}^- + H^+_{(aq)} \tag{13}$$
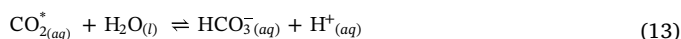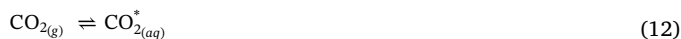
By incorporating the effect of the hydration step (Reaction (2)) and H$_2$CO$_3$ into existing equilibrium constants based on CO$_2$* (denoted by asterisk in the discussion below) it can be shown that:

$$H_{CO_2}^* e^{\left(\int_{P_{ws}}^{P} \frac{\overline{V}_{m,CO_2}}{RT} dP\right)} = \frac{f_{CO_2}}{a_{CO_2^*}} = \frac{f_{CO_2}}{a_{CO_2} + a_{H_2CO_3}} = \frac{f_{CO_2}}{a_{CO_2}(1 + K_{hyd})}$$

Hence:

$$H_{CO_2} = (1 + K_{hyd}) H_{CO_2^*}^* \tag{14}$$

The $H_{CO_2^*}^*$ term in Equation (14) is the Henry's constant at water saturation pressure on the basis of CO$_2$* concentration, which can be obtained using the expression developed by Li and Duan [51], shown in Table 3.

The fugacity coefficient of CO$_{2(g)}$, ϕ_{CO_2}, required in Equation (11), was calculated based on the empirical expression proposed by Duan et al. [52] as shown in Table 3 and it is valid for pressures up to CO$_2$ saturation pressure (P_{CO_2S} in Table 7) when $T < 305$ K and, at

Table 3
The parameters for CO$_2$/H$_2$O equilibrium calculation.*

	$\overline{V}_{m,CO_2}$ ** $(\text{cm}^3\,\text{mol}^{-1})$	$H_{CO_2^*}^*$ † [51] (bar m^{-1})	φ_{CO_2} †† [52]	K_{hyd} ‡ This study (Appendix A)	K_{ca}^* [6] ♮ (m)	K_{bi}^* [6] ♮ (m)	K_w [87] ♮♮ (m^2)	P_{ws} [88] ♭ (bar)
a_1	1.3918×10^2	1.3000×10^1	1.0000	6.6330×10^{-2}	2.3352×10^2	-1.5118×10^2	-4.0980	1.167×10^3
a_2	-6.8622×10^{-1}	-1.3341×10^{-2}	4.7587×10^{-3}	9.5260×10^3	0.0000	-8.8700×10^{-2}	-3.2452×10^3	-7.242×10^5
a_3	1.2873×10^{-3}	-5.5898×10^2	-3.3570×10^{-6}	–	-1.1974×10^4	-1.3623×10^3	2.2362	-1.707×10^1
a_4	-5.044×10^{-7}	-4.2258×10^5	0.0000	–	0.0000	0.0000	-3.984×10^7	1.202×10^5
a_5	–	–	-1.3179	–	-3.6506×10^1	2.7798×10^1	1.3957×10^1	-3.233×10^6
a_6	–	–	-3.8389×10^{-6}	–	-4.5080×10^2	-2.9515×10^1	8.5641×10^5	1.492×10^1
a_7	–	–	0.0000	–	2.1313×10^4	1.3890×10^3	–	-4.823×10^3
a_8	–	–	2.2815×10^{-3}	–	6.7143×10^1	4.4196	–	4.051×10^5
a_9	–	–	0.0000	–	8.4000×10^{-3}	3.2000×10^{-3}	–	-2.386×10^{-1}
a_{10}	–	–	0.0000	–	-4.0150×10^{-1}	-1.6440×10^{-1}	–	6.502×10^2
a_{11}	–	–	0.0000	–	-1.2000×10^{-3}	-5.0000×10^{-4}	–	–

* The a_i values are rounded to four digits after the decimal.

**. $\overline{V}_{m,CO_2} = a_1 + a_2 T + a_3 T^2 + a_4 T^3$

†.$\ln(H_{CO_2^*}^*) = a_1 + a_2 T + \frac{a_3}{T} + \frac{a_4}{T^2}$

††.$\phi_{CO_2} = a_1 + \left[a_2 + a_3 T + \frac{a_4}{T} + \frac{a_5}{T-150}\right]P + \left[a_6 + a_7 T + \frac{a_8}{T}\right]P^2$

‡.$K_{hyd} = a_1 e^{\left(-\frac{a_2}{RT}\right)}$

♮.$\ln(par.) = a_1 + a_2 T + \frac{a_3}{T} + \frac{a_4}{T^2} + a_5\ln(T) + \left(\frac{a_6}{T} + \frac{a_7}{T^2} + \frac{a_8}{T}\ln T\right) + \left(\frac{a_9}{T} + \frac{a_{10}}{T^2} + \frac{a_{11}}{T}\ln T\right)(p - p_s)^2$

$P_s = 1$ if $T < 373.15$, $P_s = P_{ws}$ if $T > 373.15$.

♮♮.$-\log(K_w) = a_1 + \frac{a_2}{T} + \frac{a_3}{T^2} + \frac{a_4}{T^3} + \left(a_5 + \frac{a_6}{T} + \frac{a_7}{T^2}\right)\log(10^{-3}\rho_w)$

$P_{ws} = 10^{\left[\frac{2C}{-B+(B^2-4AC)^{0.5}}\right]^4}$

♭$A = \theta^2 + a_1\theta + a_2$; $B = a_3\theta^2 + a_4\theta + a_5$; $C = a_6\theta^2 + a_7\theta + a_8$; $\theta = T + \frac{a_9}{T-a_{10}}$

Table 4

Equilibrium relationships for the CO2/H2O system in acidic and alkaline environments.

Reaction (2)	$\dfrac{a_{H_2CO_3(aq)}}{a_{CO_2(aq)}a_{H_2O}} = K_{hyd}$	(67)
Reaction (3)	$\dfrac{a_{HCO_3^-(aq)}a_{H^+(aq)}}{a_{H_2CO_3(aq)}} = K_{ca}$	(68)
Reaction (4)	$\dfrac{a_{CO_3^{2-}(aq)}a_{H^+(aq)}}{a_{HCO_3^-(aq)}} = K_{bi}$	(69)
Reaction (5)	$\dfrac{a_{OH^-(aq)}a_{H^+(aq)}}{a_{H_2O}} = K_w$	(70)
Reaction (41)	$\dfrac{a_{HCO_3^-(aq)}}{a_{CO_2(aq)}a_{OH^-(aq)}} = K_{ca} \times K_{hyd}/K_w$	(71)
Reaction (42)	$\dfrac{a_{CO_3^{2-}(aq)}a_{H_2O}}{a_{HCO_3^-(aq)}a_{OH^-(aq)}} = K_{bi}/K_w$	(72)

$305 < T\,(K) < 405$ up to $P = 75 + (T - 305) \times 1.25$ bar.

Following the dissolution step, the dissolved CO_2 is involved in a series of homogeneous reactions as shown via Reactions (2) through (4). Using a generic notation, any reaction j, with n_r reactants (R) and n_p products (P) can be written in the form of:

$$\sum_{m=1}^{n_r} R_m \rightleftharpoons \sum_{n=1}^{n_p} P_n \tag{15}$$

and the chemical equilibrium for this reaction can be expressed as:

$$\frac{\prod_{n=1}^{n_p} a_{P_n}}{\prod_{m=1}^{n_r} a_{R_m}} = \frac{k_{f,j}}{k_{b,j}} = K_j \tag{16}$$

The mathematical relationships expressing CO_2/H_2O equilibria expressed in terms of chemical activity of the involved species are listed in Table 4, where: $a_i = m_i\gamma_i$.

Similar to the case for Henry's constant, the equilibrium constant of H_2CO_3 dissociation reaction is commonly reported in terms of CO_2* (Reaction (13)), which is a combined parameter that includes the equilibrium constant of both CO_2 hydration and H_2CO_3 dissociation reactions. A simple mathematical manipulation based on the definition of equilibrium constants reveals the relationship between K_{Ca}^*, K_{hyd}, and K_{Ca}, where K_{Ca}^*, is the equilibrium constant of Reaction (13), and K_{Ca} is the true dissociation constant of H_2CO_3 as shown via Reaction (3):

$$K_{Ca}^* = \frac{a_{HCO_3^-(aq)}a_{H^+(aq)}}{a_{CO_2^*(aq)}} = \frac{a_{HCO_3^-(aq)}a_{H^+(aq)}}{a_{CO_2(aq)} + a_{H_2CO_3(aq)}} = \frac{a_{HCO_3^-(aq)}a_{H^+(aq)}}{a_{H_2CO_3(aq)}\left(1 + 1/K_{hyd}\right)}$$

Hence:

$$K_{Ca} = \left(1 + 1/K_{hyd}\right)K_{Ca}^* \tag{17}$$

Equation (17) shows that the known value of either K_{Ca} or K_{hyd} alongside with the known K_{Ca}^* can be used to obtain the third parameter

Considering the uncertainties in the reported values of K_{hyd} in the literature, this parameter is re-evaluated in the present study (Table 3) as discussed in Appendix A. The temperature-pressure dependence relationships developed by Li and Duan [6,51], describing the equilibrium constant of H_2CO_3 dissociation on the basis of CO_2* concentration ($K_{Ca}*$) and HCO_3^- dissociation equilibrium constant (K_{bi}), was used in the present study and is shown in Table 3. The water dissociation equilibrium, Reaction (5), is mathematically described as shown in Table 4, where K_w is the equilibrium constant (shown in Table 3) and a_{H_2O} is the activity of water that can be assumed to be unity in ideal solutions.

In addition to the above-mentioned mathematical expressions that represent the CO_2/H_2O equilibria, in the absence of an electric field the concentration of ions must also satisfy the charge balance as shown by Equation (18). The equation is commonly known as the electro-

neutrality constraint and is of fundamental importance in defining the solution speciation in the presence of ionic species.

$$\sum_i z_i m_i = 0 \tag{18}$$

Additional cations and anions in the solution may alter the speciation from the "natural" state of a pure H_2O/CO_2 system. This can be due to the change in activity coefficients in the presence of a significant amount of a dissolved species. The effect of neutral salts such as chloride salts (e.g. NaCl, KCl) on the solution speciation is an example of such a scenario. In addition to the effect on activity coefficients, the presence of ions may change the speciation by altering the charge balance in the solution, as described by the electroneutrality equation. This is the case when the additional species include an ion that is involved in the chemical equilibrium of the system, coupled with a "conserved" ion. The conserved ions (e.g. Na^+, Ca^{2+}, Cl^-) are not involved in chemical equilibrium of H_2O/CO_2 system and their concentration is not directly affected by the environmental conditions, pCO$_2$ and the solution pH. Such chemical compounds can be grouped as either acids (e.g. hydrochloric acid), bases (e.g. sodium hydroxide), or acidic/alkaline salts (e.g. carbonate, and bicarbonate salts). As a generic rule, the concentration of the ions involved in the chemical equilibria are bound to compensate for any charge imbalance (C.I. in the following text) of the conserved ions.

2.2.1.1. Non-ideal aqueous phase. In dilute solutions, it can be assumed that activity coefficients are close to unity, however, as the concentration of dissolved species increases, this assumption may result in significant miscalculation of the equilibrium speciation. In the present study, the activity coefficients are obtained using the well-known Pitzer's specific interaction equations. This approach is commonplace in calculation of activity coefficients of complex electrolytes with high ionic strength and has been used extensively for H_2O/CO_2 systems containing various ionic species. Based on Pitzer's equations, the activity coefficients of cations (M), anions (X), and neutral species (N) can be calculated via Equations (19)–(21), respectively. In these equations the molality of species is denoted by m, with subscripts c and a corresponding to cations and anions, respectively, and z denoting the charge of any given ion.

$$\begin{aligned}
ln(\gamma_M) = z_M^2 F &+ \sum_{a=1}^{N_a} m_a (2B_{Ma} + ZC_{Ma}) + \sum_{c=1}^{N_c} m_c \left(2\Phi_{Mc} + \sum_{a=1}^{N_a} m_a \psi_{Mca}\right) \\
&+ \sum_{a=1}^{N_a-1} \sum_{a'=a+1}^{N_a} m_a m_{a'} \psi_{aa'M} + |z_M| \sum_{c=1}^{N_c} \sum_{a=1}^{N_a} m_c m_a C_{ca} + \sum_{n=1}^{N_n} 2m_n \lambda_{nM}
\end{aligned} \tag{19}$$

$$\begin{aligned}
ln(\gamma_X) = z_X^2 F &+ \sum_{c=1}^{N_c} m_c (2B_{cX} + ZC_{cX}) + \sum_{a=1}^{N_a} m_a \left(2\Phi_{Xa} + \sum_{c=1}^{N_c} m_c \psi_{Xac}\right) \\
&+ \sum_{c=1}^{N_c-1} \sum_{c'=c+1}^{N_c} m_c m_{c'} \psi_{cc'X} + |z_X| \sum_{c=1}^{N_c} \sum_{a=1}^{N_a} m_c m_a C_{ca} + \sum_{n=1}^{N_n} 2m_n \lambda_{nX}
\end{aligned} \tag{20}$$

$$ln(\gamma_N) = \sum_{n=1}^{N_n} 2m_n \lambda_{Nn} + \sum_{c=1}^{N_c} 2m_c \lambda_{Nc} + \sum_{a=1}^{N_a} 2m_a \lambda_{Na} + \sum_{c=1}^{N_c} \sum_{a=1}^{N_a} m_c m_a \xi_{Nca} \tag{21}$$

Furthermore, the activity of water, as the solvent, is defined via:

$$ln(a_{H_2O}) = -\frac{MW_{H_2O}\,\phi}{1000} \sum_i m_i \tag{22}$$

with molecular weight of water, $MW_{H_2O} = 18.015$, and the osmotic pressure (φ) obtained through Equation (23):

$$(\phi - 1) = \frac{2}{\sum_i m_i}\left(-\frac{A^\phi I^{3/2}}{1 + b\,I^{1/2}}\right)\left[\sum_{c=1}^{N_c}\sum_{a=1}^{N_a} m_c m_a (B_{ca}^\phi + Z C_{ca})\right.$$

$$+ \sum_{c=1}^{N_c-1}\sum_{c'=c+1}^{N_c} m_c m_{c'}\left(\Phi_{cc'}^\phi + \sum_{a=1}^{N_a} m_a\,\psi_{cc'a}\right)$$

$$+ \sum_{a=1}^{N_a-1}\sum_{a'=a+1}^{N_a} m_a m_{a'}\left(\Phi_{aa'}^\phi + \sum_{c=1}^{N_c} m_c\,\psi_{aa'c}\right) + \sum_{n=1}^{N_n}\sum_{a=1}^{N_a} m_n m_a \lambda_{na}$$

$$\left. + \sum_{n=1}^{N_n}\sum_{c=1}^{N_c} m_n m_c \lambda_{nc} + \sum_{n=1}^{N_n}\sum_{c=1}^{N_c}\sum_{a=1}^{N_a} m_n m_c m_a \xi_{nca}\right] \tag{23}$$

The parameters F, and Z appearing in Equations (19), (20), and (23) are defined as:

$$F = -A^\phi\left(\frac{I^{1/2}}{1 + b\,I^{1/2}} + \frac{2}{b}\ln\left(1 + b\,I^{1/2}\right)\right) + \sum_{c=1}^{N_c}\sum_{a=1}^{N_a} m_c m_a B_{ca}'$$

$$+ \sum_{c=1}^{N_c-1}\sum_{c'=c+1}^{N_c} m_c m_{c'}\Phi_{cc'}' + \sum_{a=1}^{N_a-1}\sum_{a'=a+1}^{N_a} m_a m_{a'}\Phi_{aa}' \tag{24}$$

$$Z = \sum_i |z_i|\,m_i \tag{25}$$

where A^ϕ is one third of the Dubye–Huckel limiting slope with value of 0.392 at 25 °C. A^ϕ is discussed in detail by Pitzer [53] and it was shown to have a $-3/2$ order temperature dependence, hence:

$$A^\phi = 0.392\left(\frac{298.15}{T}\right)^{3/2} \tag{26}$$

The parameter B appearing in Equations (19) and (20), B^ϕ in Equation (23), and B' in Equation (24), are the second virial coefficients representing the interaction of opposite charge ions, which are obtained via the following ionic strength (I) dependent relationships:

$$B_{MX}^\phi = \beta_{MX}^{(0)} + \beta_{MX}^{(1)}\,e^{-a_{MX}\sqrt{I}} + \beta_{MX}^{(2)}\,e^{-12\sqrt{I}} \tag{27}$$

$$B_{MX} = \beta_{MX}^{(0)} + \beta_{MX}^{(1)}\,g(a_{MX}\sqrt{I}) + \beta_{MX}^{(2)}\,g(12\sqrt{I}) \tag{28}$$

$$B_{MX}' = \beta_{MX}^{(1)}\,g'(a_{MX}\sqrt{I})/I + \beta_{MX}^{(2)}\,g'(12\sqrt{I})/I \tag{29}$$

where $\beta^{(0)}$, $\beta^{(1)}$, and $\beta^{(2)}$ are the parameters obtained experimentally (see Appendix B), $a_{MX} = 2.0$ when M or X is a univalent ion, or $a_{MX} = 1.4$ when X and M are $2-2$ or higher valance couple. The functions $g(x)$ and $g'(x)$ are defined as:

$$g(x) = 2(1 - (1 + x)e^{-x})/x^2 \tag{30}$$

$$g'(x) = -2\left(1 - \left(1 + x + \frac{x^2}{2}\right)e^{-x}\right)/x^2 \tag{31}$$

The second virial coefficients, Φ, Φ^ϕ, and Φ', appearing in Equations (19), (20), (23), and (24), represent the interaction of same charged ions, and they can be obtained via:

$$\Phi_{ij}^\phi = \theta_{ij} + E_{\theta_{ij}}(I) + I\,E_{\theta_{ij}}'(I) \tag{32}$$

$$\Phi_{ij} = \theta_{ij} + E_{\theta_{ij}}(I) \tag{33}$$

$$\Phi_{ij}' = E_{\theta_{ij}}'(I) \tag{34}$$

The value of θ_{ij} is obtained experimentally (see Appendix B), and the functions $E_{\theta_{ij}}$ and $E_{\theta_{ij}}'$ are defined via Equations (35) and (36), respectively.

$$E_{\theta_{ij}} = \left(\frac{z_i z_j}{4I}\right)\left[J(x_{ij}) - \frac{1}{2}J(x_{ii}) - \frac{1}{2}J(x_{jj})\right] \tag{35}$$

$$E_{\theta_{ij}}' = -\left(E_{\theta_{ij}}\big/I\right) + \left(z_i z_j\big/8I^2\right)\left[x_{ij}\,J'(x_{ij}) - \frac{1}{2}x_{ii}\,J'(x_{ii}) - \frac{1}{2}x_{jj}\,J'(x_{jj})\right] \tag{36}$$

The value of the function J, and its derivative $J' = dJ/dx$, were evaluated by Pitzer [53] and shown to be reasonably represented with the empirical Equation (37), with $C_1 = 4.581$, $C_2 = 0.7237$, $C_3 = 0.0120$, $C_4 = 0.528$.

$$J = x[4 + C_1 x^{-C_2}\exp(-C_3 x^{C_4})]^{-1} \tag{37}$$

The second virial coefficients, λ_{ni}, appearing in equations (19), (20), (21), and (23), represent the interaction of a neutral species, and it is obtained experimentally similar to parameters θ and β (see Appendix B).

The parameters C, ψ, ζ, appearing in Equations (19), (20), (21), and (23), are the third virial coefficients. C_{MX}, representing the single electrolyte interaction, can be obtained via Equation (38):

$$C_{MX} = \frac{C_{MX}^\phi}{2}\,|z_M z_X|^{0.5} \tag{38}$$

The parameters, C_{MX}^ϕ, ψ, and ζ, are obtained experimentally. The parameters of the second and third virial coefficients required for calculation of the activity coefficients were extracted from the literature and are listed in Appendix B.

2.2.1.2. Speciation calculation. The discussion in the previous section lays out the relationships involved in water chemistry calculations, including the equilibrium equations shown in Table 4, along with the electroneutrality constraint and the mathematical relationships required for calculation of activity coefficients. Depending on the known parameters such as the fugacity of CO_2 in the gas phase, solution pH, etc. these equations can be arranged and solved to obtain the solution speciation. These equations form a set of non-linear, coupled algebraic equations that can be expressed using matrix notation in the form of Equation (39), where [A] is a square coefficient matrix, [C] is a vector of the unknown concentrations, and S is the vector of the source terms. The unknown concentration vector ([C]) can then be obtained by calculating the inverse coefficient matrix as shown in Equation (40). In some cases, especially for solution speciation calculation in non-ideal conditions where the coefficient matrix is dependent on the unknown concentration of species iterative solution schemes are required.
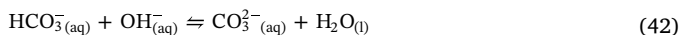
$$[A].\,[C] = [S] \tag{39}$$

$$[C] = [A]^{-1}.\,[S] \tag{40}$$

2.2.2. Chemical kinetics of the H_2O/CO_2 system

In internal pipeline corrosion, the solution speciation in the boundary layer may deviate from that in the bulk, under the influence of heterogeneous reactions at the metal surface. The heterogeneous reactions include both the electrochemical reactions causing the metal deterioration and the chemical reactions, such as corrosion product layer formation. The concentration of the species at the metal surface defines (in part) the rate of electrochemical reactions and, hence, it is essential for determining the corrosion rate. Such calculations require the explicit knowledge of the kinetics of the involved homogeneous chemical reactions.

The homogeneous chemical reactions in the acidic CO_2/H_2O system are listed above as Reactions (1) through (5). However, the hydroxylation reactions of the carbonate species as shown via Reactions (41) and (42) may also become significant in near-neutral and alkaline environments. It is worthwhile to note that Reactions (41) and (42) are the equivalents of Reactions (3) and (4) with addition of water dissociation, hence, if the conditions of the equilibrium for those reactions are satisfied, Reactions (41) and (42) are also at equilibrium. In other words the relationships describing the equilibrium of Reactions (41) and (42) are not independent equations from the set describing the CO_2 speciation in acidic solutions. Hence, they are not included in equilibrium water chemistry calculation. Nevertheless, these "alkaline"

reactions can be of significance when it comes to the reaction kinetics and are discussed in more detail in the following paragraphs.

$$CO_{2(aq)} + OH^-_{(aq)} \leftrightharpoons HCO^-_{3(aq)} \tag{41}$$

$$HCO^-_{3(aq)} + OH^-_{(aq)} \leftrightharpoons CO^{2-}_{3(aq)} + H_2O_{(l)} \tag{42}$$

The rate of production or consumption of each species can be calculated by considering the forward and backward rates of all the homogeneous reactions. The rate of each chemical reaction j involved in the generic Reaction (43) can be calculated as shown in Equation (44).

$$\sum_{r=1}^{n_r} C_r \rightleftharpoons \sum_{p=1}^{n_p} C_p \tag{43}$$

$$R_j = k_{f,j} \prod_{r=1}^{n_r} C_r - k_{b,j} \prod_{p=1}^{n_p} C_p \tag{44}$$

The reaction rate of chemical species i involved in the chemical reactions can be summarized in a matrix format as shown in Equation (45). Where the coefficient matrix has the size of $i \times j$, i being the number of chemical species and j being the number of chemical reactions.

$$
\begin{bmatrix}
R_{CO_{2(aq)}} \\
R_{H^+_{(aq)}} \\
R_{H_2CO_{3(aq)}} \\
R_{HCO^-_{3(aq)}} \\
R_{CO^{2-}_{3(aq)}} \\
R_{OH^-_{(aq)}}
\end{bmatrix}
=
\begin{bmatrix}
-1 & 0 & 0 & 0 & -1 & 0 \\
0 & 1 & 1 & 1 & 0 & 0 \\
1 & -1 & 0 & 0 & 0 & 0 \\
0 & 1 & -1 & 0 & 1 & -1 \\
0 & 0 & 1 & 0 & 0 & 1 \\
0 & 0 & 0 & 1 & -1 & -1
\end{bmatrix}
$$

$$
\times
\begin{bmatrix}
k_{f,hyd}\, a_{CO_2} a_{H_2O} - k_{b,hyd}\, a_{H_2CO_3} \\
k_{f,ca}\, a_{H_2CO_3} - k_{b,ca}\, a_{H^+} a_{HCO_3^-} \\
k_{f,bi}\, a_{HCO_3^-} - k_{b,bi}\, a_{H^+} a_{CO_3^{2-}} \\
k_{f,w}\, a_{H_2O} - k_{b,w}\, a_{H^+} a_{OH^-} \\
k_{f,hyd,OH}\, a_{CO_2} a_{OH^-} - k_{b,hyd,OH}\, a_{HCO_3^-} \\
k_{f,bi,OH}\, a_{HCO_3^-} a_{OH^-} - k_{b,bi,OH}\, a_{CO_3^{2-}} a_{H_2O}
\end{bmatrix}
\tag{45}
$$

The kinetic rate constants of the chemical reactions of CO_2/H_2O system, used in Equation (45), are listed in Table 5. Eigen [54,55] characterized the protonation reactions of bicarbonate, carbonate and hydroxide ion as being "diffusion limited", meaning that these reactions are virtually instantaneous when the hydrogen ion and any of the these anions are encountered. The value of 4.7×10^{10} ($M^{-1} s^{-1}$) suggested for bicarbonate protonation, and the $pK_a = 3.49$ for H_2CO_3 dissociation, shows that the H_2CO_3 dissociation rate constant is of the order of 10^7 (s^{-1}). Such a large kinetic rate constant suggests that the kinetics of H_2CO_3 dissociation is not rate limiting in the typical conditions encountered in CO_2 corrosion scenarios. On the other hand, water dissociation with pK_a of 14, and protonation rate constant of 1.4×10^{11} ($M^{-1} s^{-1}$), has a kinetic rate constant of the order of 10^{-3} (s^{-1}),

Table 5
Kinetic rate constants for reactions involved in CO_2/H_2O system. k_f denotes the reaction progress from left to right.

Reaction #	Reaction rate constant	Reference
(2)	$k_{b,hyd} = 4.86 \times 10^{12} e^{\left(\frac{-64485}{RT}\right)}$ (s^{-1})	This study (Appendix A)
(3)	$k_{b,ca} = 4.7 \times 10^{10}$ ($M^{-1} s^{-1}$)	[54]
(4)	$k_{f,bi} = 2.03 \times 10^7 e^{\left(\frac{-35269}{RT}\right)}$ (s^{-1})	This study
(5)	$k_{b,w} = 1.12 \times 10^{11}$ ($M^{-1} s^{-1}$)	[89]
(41)	$k_{f,hyd,OH} = 4.2 \times 10^{13} e^{\left(\frac{-55438}{RT}\right)}$ ($M^{-1} s^{-1}$)	[56]
(42)	$k_{f,bi,OH} = 6 \times 10^9$ ($M^{-1} s^{-1}$)	[54]

suggesting that this reaction is very slow. The rate constant for bicarbonate dissociation is determined to be 13.4 (s^{-1}) at 25 °C in the present study (more details are given in Section 3.4), which places the kinetics of this reaction in between the two above "extreme" cases: the very slow water dissociation and the very fast H_2CO_3 dissociation. This value suggests that the kinetics of bicarbonate dissociation reaction can become the determining factor in corrosion rate prediction at certain conditions. The authors were unable to find any experimental measurements of this kinetic parameter in the literature for further confirmation of the values obtained in the present study. Nevertheless, Zeebe and Wolf-Gladrow reported the theoretically estimated value of 5×10 ($M^{-1} s^{-1}$) for carbonate ion protonation reaction rate constant, which by considering the pK_a of 10.32 for HCO3- [2] results in a dissociation rate constant of 2.3 (s^{-1}), what is about one order of magnitude smaller than the value determined in the present study.

As noted above, Reactions (41) and (42) are significant only in near-neutral and alkaline solutions. When discussing the homogeneous chemical reaction kinetics these two reactions should be accounted for as they may provide parallel pathways for consumption or production of the involved chemical species.

The reaction of CO_2 with OH^- (Reaction (41)) occurs in parallel to the CO_2 hydration reaction. The rate constant for Reaction (41) has been determined by Pinsent et al. [56] as noted in Table 5, and was shown to agree reasonably well with the results obtained from other independent studies [57,58]. At 25 °C the rate constant of the CO_2 hydroxylation reaction is 8.04×10^3 ($M^{-1} s^{-1}$). At the same condition, the rate constant of CO_2 hydration reaction is 3.33×10^{-2} (s^{-1}). The comparison of the rate of these reactions suggest that the "crossover" occurs at pH 8.62, assuming an ideal solution:

$$k_{f,hyd}\, c_{CO_2} = k_{f,hyd,OH}\, c_{CO_2} c_{OH^-}$$

$$pH = 14 - \log\left(\frac{k_{f,hyd}}{k_{f,hyd,OH}}\right) = 8.62$$

This suggests that at pH values about 8 both reactions are of significance and should be included in calculations. Note that while CO_2 corrosion is generally defined in acidic solutions, such high pH values can be reached in the vicinity of the metal surface when the cathodic current is under mass transfer control specially when the bulk solution has a pH ≥ 6.

The hydroxylation of HCO_3^-, forward partial of Reaction (42), is also categorized as "diffusion limited" [54], with the reaction rate of 6×10^9 ($M^{-1} s^{-1}$) at 25 °C. The comparison of the rate of this reaction with that of bicarbonate dissociation, shows that the "crossover" of the rates of these two reactions is at ~pH = 5, suggesting that these reactions are kinetically of equal significance at nearly all typical conditions encountered in industrial CO_2 corrosion scenarios.

$$k_{f,bi,OH}\, c_{HCO_3^-} c_{OH^-} = k_{f,bi}\, c_{HCO_3^-}$$

$$pH = 14 - \log\left(\frac{k_{f,bi,OH}}{k_{f,bi}}\right) = 5.12$$

2.2.3. Electrochemical reactions

The rate of electrochemical reactions at the metal surface were expressed in the same fashion as discussed in our earlier study [35]. The carbonic species are not considered to be electrochemically active as far as the cathodic currents are concerned (neither H_2CO_3 nor HCO_3^- reduction). Also, the water reduction reaction is not considered to be significant in the vicinity of the corrosion potential, considering that it occurs at an appreciable rate only at much more negative potentials. The sole cathodic reaction in the present model is the H^+ reduction, with the rate expressed via Equation (46).

$$i_c = -Fk_{0H^+} a^s_{H^+}{}^{m_{H^+}} e^{\left(\frac{\alpha FE}{RT}\right)} \tag{46}$$

where i_c is the cathodic current density in A m², $a^s_{H^+}$ is the surface

activity of hydrogen ions, m_{H^+} is the apparent reaction order, and other parameters have their common electrochemical meaning. The kinetic parameters of the H^+ reduction reaction were obtained by the best fit of the model with the experimental data: $k_{0H^+} = 2 \times 10^{-8}$, $m_{H^+} = 0.5$, $\alpha_{H^+} = 0.43$, as shown below in Section 3.

The rate of the iron oxidation reaction in the active dissolution, transition, and pre-passivation ranges can be obtained as the combination of three different rate determining steps considering the surface coverage by an intermediate species θ, according to Equations (47)–(49), as discussed in details elsewhere [35]. This approach accounts for the known change of the governing mechanism and the kinetics of iron dissolution from active dissolution to transition and pre-passivation as a function of potential and pH. In comparison to earlier methods where a discontinued set of kinetic parameters were used to represent this change of mechanism at the vicinity of corrosion current for various pH values [11,19], Equation (47) allows for a smooth transition in-between the governing mechanisms. Furthermore, the observed effect of the pCO_2 on the kinetics of the iron dissolution at the transition and pre-passivation ranges are accounted for in Equation (47).

$$i_a = \left(\frac{1}{(1-\theta)i_1} + \frac{1}{(1-\theta)i_2} \right)^{-1} + \theta i_3 \tag{47}$$

$$i_{a,j} = F k_{0,j} a_{H^+}^{s\,m_{H^+,j}} a_{CO_2}^{s\,m_{CO_2,j}} e^{\left(\frac{\alpha_j FE}{RT} \right)} \tag{48}$$

$$\theta = \frac{K_\theta a_{H^+}^{s\,m_{H^+,\theta}} a_{CO_2}^{s\,m_{CO_2,\theta}} e^{\left(\frac{\alpha_\theta FE}{RT} \right)}}{1 + K_\theta a_{H^+}^{s\,m_{H^+,\theta}} a_{CO_2}^{s\,m_{CO_2,\theta}} e^{\left(\frac{\alpha_\theta FE}{RT} \right)}} \tag{49}$$

The kinetic parameters for these reactions were also obtained based on the best fit of the model to the experimental data as shown below:

a, 1: $k_{0,1} = 4.0 \times 10^9$; $m_{H^+,1} = -2.5$; $m_{CO_2,1} = 0$; $q_1 = 2.5$

a, 2: $k_{0,2} = 1.0 \times 10^{13}$; $m_{H^+,2} = 1$; $m_{CO_2,2} = 0.5$; $q_2 = 2$

a, 3: $k_{0,3} = 08 \times 10^{-3}$; $m_{H^+,3} = -0.5$; $m_{CO_2,3} = 0.5$; $q_3 = 0.5$

θ: $K_\theta = 5.0 \times 10^{13}$; $m_{H^+,\theta} = -2.5$; $m_{CO_2,\theta} = -0.5$; $q_\theta = 2.5$

2.2.4. Mass conservation inside the boundary layer

The rate of electrochemical reactions and consequently the corrosion rate can only be determined accurately if the surface concentration of the involved electroactive species is known. These values, in a practical sense, are not directly measurable. Nevertheless, with a known speciation in the bulk solution the values of the surface concentrations can be calculated by constructing a detailed account of their transfer through the boundary layer.

The flux of chemical species inside the diffusion boundary layer can be described by Equation (50). The mathematical model developed in the present study considers the non-ideal solution properties in the context of moderately dilute solutions, hence, the flux of species, N_i (mol m^{-3} s^{-1}), is expressed in terms of chemical potential as shown in Equation (50).

$$N_i = -u_i C_i \nabla \mu_i + C_i v \tag{50}$$

where C_i is concentration (mol m^{-3}), u_i is mobility (m^2 s^{-1} V^{-1}), v (m s^{-1}) in the second term represents the convective flow due to the movement of the bulk fluid, and μ_i (j mol^{-1}) is the electrochemical potential of the species, which can be expressed based on independent "chemical" and "electrostatic" parts [59]:

$$\mu_i = \mu_i^0 + RT \ln(\gamma_i C_i) + F z_i \phi \tag{51}$$

where μ_i^0 is the standard chemical potential, and ϕ (V) is the potential inside the solution. The combination of Equations (50) and (51), assuming that the Nernst-Einstein relationship ($D_i = RT u_i$) holds, gives

the flux relationship for non-ideal condition in moderately dilute solutions, yields:

$$N_i = -D_i \nabla C_i - D_i C_i \nabla \ln(\gamma_i) - \frac{F D_i C_i z_i}{RT} \nabla \phi + C_i v \tag{52}$$

In ideal solution conditions where γ_i approaches 1 the second term in Equation (52) collapses to zero and the flux relationship of an infinitely diluted solution is recovered [59].

In Equation (52), the bulk movement of the fluid is accounted for by the convective flow term ($C_i v$), where v describes the local velocity within the boundary layer. However, in the turbulent flow regime seen in most applications including the thin channel flow cell apparatus used here, the dominant mass transfer mechanism is in the form of turbulent mixing. The turbulent mixing can be assumed to be isotropic in the diffusion boundary layer and decays as the solid wall is approached. Due to its diffusion-like effect on species transport, it can be approximated by a diffusion equation, with a variable "eddy diffusivity" (D_e in m^2 s^{-1}), being a function of the distance from the metal surface [60,61]. Equation (52) can then be restated as following for turbulent flow regime:

$$N_i = -(D_i + D_e) \nabla C_i - D_i C_i \nabla \ln(\gamma_i) - \frac{F D_i C_i z_i}{RT} \nabla \phi \tag{53}$$

The concentration of each chemical species for an elementary volume of the solution can be determined by using a mass conservation law. The change in concentration of species i in a small control volume of size Δx over a time interval of Δt is defined by the change in flux of this species across control volume, and the source term arising from consumption/production of this species by homogeneous chemical reactions, with a rate R_i (mol m^{-3} s^{-1}). This is mathematically expressed via the three-dimensional vector Equation (54):

$$\frac{\partial C_i}{\partial t} = -\nabla \cdot N_i + R_i \tag{54}$$

In the case of uniform corrosion, the components of Equation (53) and Equation (54) in the two directions parallel to the metal surface are not of any significance as there are no gradients of concentration in those directions. Therefore, one ends up with a one-dimensional domain in the direction x normal to the metal surface, spreading throughout the boundary layer, hence, Equation (53) and Equation (54) can be simplified to scalar Equation (55) and Equation (56), respectively.

$$N_i = -(D_i + D_e)\frac{\partial C_i}{\partial x} - D_i C_i \frac{\partial \ln(\gamma_i)}{\partial x} - \frac{z_i D_i F C_i}{RT}\frac{\partial \phi}{\partial x} \tag{55}$$

$$\frac{\partial C_i}{\partial t} = \frac{\partial}{\partial x}\left((D_i + D_e)\frac{\partial C_i}{\partial x} \right) + \frac{\partial}{\partial x}\left(D_i C_i \frac{\partial \ln(\gamma_i)}{\partial x} \right) + \frac{\partial}{\partial x}\left(\frac{z_i D_i F C_i}{RT}\frac{\partial \phi}{\partial x} \right) + R_i \tag{56}$$

The activity coefficient term appearing in Equation (56) was calculated using Pitzer's model as described in the previous section, based on the local concentration of the chemical species. In order to do so, the Pitzer model developed Water Chemistry Calculation section was coupled with the electrochemical model discussed here.

The effect of homogeneous chemical reactions is expressed via R_i term in Eq. (56), which is also significantly influenced by the non-ideal solution properties. The term R_i, including the effect of activity coefficients, is calculated according to the discussion presented in the Water Chemistry Calculation section. An accurate account of the homogeneous chemical reaction rates involved in the complex water chemistry of CO_2 saturated solutions is essential for calculating the concentration of the chemical species inside the boundary layer and particularly so at the metal surface. This is of significance, since the dissociation reactions associated with weak acids such as H_2CO_3, carboxylic acids, and hydrogen sulfide may act as an additional source (or sink) of the chemical species (e.g. hydrogen ion) as their concentrations

Table 6
Reference diffusion coefficients at 25 °C.

Species	Diffusion coefficient in water $\times 10^9$ (m²/s)	Reference
CO_2	1.92	[90]
H_2CO_3	1.75	Estimated
HCO_3^-	1.185	[91]
CO_3^{2-}	0.923	[91]
H^+	9.312	[59]
OH^-	5.273	[91]
Na^+	1.334	[59]
Cl^-	2.032	[59,91]
Fe^{2+}	0.72	[59]

depart from equilibrium values. For example, the buffering effect of H_2CO_3 and HCO_3^- on the electrochemical response of the system is reflected by this term.

The effect of molecular diffusion induced by the concentration gradient of the chemical species inside the boundary layer is accounted for in the first terms of Equations (55) and (56). The diffusion coefficients for the chemical species included in the present model can be found in Table 6. The temperature dependence of the diffusion coefficient is estimated based on the Einstein-Stocks relationship as shown in Table 7.

The effect of turbulent flow accounted for by the eddy diffusivity in Equations (55) and (56). The change of eddy diffusivity in the boundary layer near the metal surface for a fully developed turbulent flow though pipes and conduits can be expressed via Equation (57), as discussed in more detail elsewhere [35,61].

$$D_e = \nu \frac{0.0007 \, x^{+3}}{[1 + 0.00405 x^{+2}]^{1/2}} \tag{57}$$

where ν is the kinematic viscosity (m² s⁻¹), and x^+ is the dimensionless distance from the wall defined as:

$$x^+ = \frac{x \left(\tau_w / \rho \right)^{1/2}}{\nu} \tag{58}$$

Equation (57) is valid for fluids with Schmidt number of one or greater, over $x^+ < 30$, and is applicable for all turbulent boundary layers when appropriate dimensionless parameters are used. The wall shear stress, τ_w in Pa, appearing in Equation (58) can be calculated as:

$$\tau_w = \frac{1}{2} \rho C_f V^2 \tag{59}$$

where ρ (kg m⁻³) is water density and V (m s⁻¹) is the average water velocity. The term C_f in Equation (59) is the flow geometry dependent Fanning friction factor, which can be calculated based on the explicit relationship reported by Swamee and Jain [62] for the Darcy friction factor (C_d), considering $C_d = 4C_f$.

Table 7
Temperature dependence of the physiochemical properties.

Parameter	Relationship	Reference
Water density (kg/m³)	$\rho_w = 753.596 + 1.87748 \, T - 0.003562 \, T^2$	[19]
Water viscosity (cP)	$\mu = \mu_{ref} 10^{\left(\frac{1.1709 \, (T_{ref} - T) - 0.001827 (T_{ref} - T)^2}{(T - 273.15) + 89.93} \right)}$ $T_{ref} = 293.15 \, K, \; \mu_{ref} = 1.002 \, cP$	[92]
Diffusion coefficient *	$D_i = D_{i,ref} \frac{T}{T_{ref}} \frac{\mu_{ref}}{\mu}$	
Saturation pressure of CO_2 (mm Hg)	$\log(P_{CO_2 S}) = 7.58828 - \frac{861.82}{(T - 273.15) + 271.883}$	[93]
* Reference values are listed in Table 6.		

$$C_d = 0.25 \left[\log \left(\frac{\varepsilon / D_{eq}}{3.7} + \frac{5.74}{Re^{0.9}} \right) \right]^{-2} \tag{60}$$

where ε (m) is the surface roughness (assumed to be negligible in the present study). For the present case of thin channel flow, the Reynolds number ($Re = V \, D_{eq} / \nu$) was calculated based on the equivalent diameter: $D_{eq} = 4A/P$ (m), with A and P being the cross-section area and the interior perimeter of the thin channel, respectively. Equation (60) is merely an explicit version of the well-known Colebrook–White correlation [63].

The effect of electromigration on the flux of ionic species away/towards the metal surface is accounted for by the third term of Equations (55) and (56). While its contribution to the surface concentration of electroactive species in the brines with high ionic strength is negligible, in certain corrosion scenarios it cannot be neglected. For example, in the case of corrosion in condensed water such as seen in Top of the Line Corrosion (TLC) or corrosion inside "dry" gas lines, the liquid phase does not include any significant amount of dissolved salts (e.g. NaCl). The calculation of the electro-migration effect requires the potential inside the boundary layer to be specified. This parameter can be obtained by the aid of the electro-neutrality constraint as an additional relationship (Equation (61)):

$$\sum_i z_i C_i = 0 \tag{61}$$

2.2.5. Initial and boundary conditions

Since Equation (56) is a transient partial differential equation, the initial and boundary conditions need to be defined. At the initial time ($t = 0$) it can be assumed that the well mixed solution comes into contact with the metal surface. Hence, the concentrations of all chemical species throughout the diffusion layer are constant, known values, defined by the chemical equilibria of the solution.

In the bulk solution ($x = \delta$) the concentration of chemical species remains unchanged at all times ($t \geq 0$). Therefore, for the bulk solution, the boundary condition can be defined based on the known concentration of species being identical to the initial conditions.

The boundary condition at the metal/solution interface is based on the known fluxes of species and includes all the electrochemical reaction rate calculations. For an electroactive chemical species, the flux at the metal/solution boundary is equal to the rate of the corresponding electrochemical reactions. For an electroactive species i, involved in electrochemical reaction j, the flux at the metal surface can be described through equation (62):

$$N_i|_{x=0} = - \frac{s_{ij} i_j}{n_j F} \tag{62}$$

The negative sign in Equation (62) is due to a sign convention where cathodic currents are presumed to be negative and anodic currents are positive. Additionally, the reactants of an electrochemical reaction are represented with a negative stoichiometric coefficient (s_{ij}) and the products with a positive one.

For non-electroactive species, the flux at the metal surface is zero:

$$N_i|_{x=0} = 0 \tag{63}$$

Equation (62) and Equation (63) can be applied to describe the flux for all chemical species at the metal surface. The electric potential inside the solution may also be specified through the electroneutrality constraint via Equation (61).

Considering the governing equations, the initial conditions, and the boundary conditions discussed above, this system of equations is fully specified if the potential at the metal surface (E) is known so that the rate of electrochemical reactions can be calculated. That is a common case in electroanalytical measurements (e.g. potentiodynamic sweeps) where electrode potential is the controlled parameter. However, in corrosion rate predictions: $E = E_{cor}$ (corrosion potential) and is not

Table 8
Summary of equations used in the comprehensive mathematical model.

Electrode surface boundary

$N_i = - \sum_j \frac{s_{ij} i_j}{n_j F}$ for all electroactive species

$N_i = 0$ for all n on-electroactive species

$\sum_i z_i C_i = 0$

$i_{app} = 0 = \sum_j i_j$ for unknown electrode potential case

---

Diffusion boundary layer

$\frac{\partial C_i}{\partial t} = \frac{\partial}{\partial x}\left((D_i + D_e)\frac{\partial C_i}{\partial x} \right) + \frac{\partial}{\partial x}\left(D_i C_i \frac{\partial \ln(\gamma_i)}{\partial x} \right) + \frac{\partial}{\partial x}\left(\frac{z_i D_i F C_i}{RT}\frac{\partial \phi}{\partial x} \right) + R_i$

$\sum_i z_i C_i = 0$

Bulk boundary and Initial condition

$C_i = C_i^b$ for all species

$\Phi = 0$

---

known a priori. In that case, the charge conservation at the metal surface can serve as an additional equation required to obtain E. All the cathodic currents are balanced by the anodic currents, meaning that the net current resulting from all j electrochemical reactions is equal to zero (i.e. there is no externally "applied" current i_{app}). The charge conservation can be mathematically expressed as Equation (64).

$$i_{app} = 0 = \sum_j i_j \qquad (64)$$

2.2.6. Mathematical methods

The mathematical equations as summarized in Table 8 form a set of transient non-linear, coupled, partial differential equations that need to be solved numerically. The solution here was obtained using a non-uniform grid and the finite difference method based on Newman's "Band-J" open source code [59,64], similar to what is described in our

earlier studies [27,35,65].

In the present study, the electrochemical model as described above was coupled with the water chemistry Pitzer model in order to include the effect of non-ideal solutions in a computationally reasonable time. The inputs of the model include the solution pH, NaCl concentration, temperature, CO_2 partial pressure, flow velocity, hydrodynamic characteristic length, the number and size of spatial and temporal nodes, and the potential range, if applicable. As the first step, the solution speciation was obtained based on the water chemistry model. The results were used to specify the initial and the bulk boundary conditions of the electrochemical model. Considering the non-linear equations in the electrochemical model, and also in the coupled Pitzer model, the solution was obtained using an iterative calculation approach. The concentrations and activity coefficients for the bulk solution was used

as the first guess to solve the equations at the first temporal node and all spatial nodes. The results were then used as input for the Pitzer model to obtain a new set of local activity coefficients. The process was iterated until convergence with a reasonable accuracy is achieved. At the end of this process, the concentrations and the activity coefficients at all spatial nodes were specified. Then the time was advanced, and the same process repeated for the following time steps, using the last set of concentrations and activity coefficients as the initial guess.

3. Results and discussion

3.1. Speciation calculation

Following the discussion in the water chemistry section the coefficient matrix can be developed as shown in Equation (65) to represent the experimental conditions of the present study. Here Na^+ and Cl^- are the only two conserved ions present in the solution and pCO_2 and the solution pH are known. In addition to that from a neutral salt i.e. NaCl ($c_{NaCl_{(aq)}}$), these ions were also introduced in the solution as HCl, NaOH, or $NaHCO_3$, to adjust the solution pH. Here the parameter "C.I." with units of concentration is introduced to represent the Charge Imbalance at the specified pH, which is assumed to be in the form of Na^+ ions here, i.e. the addition of NaOH or $NaHCO_3$ into the solution. This parameter is commonly referred to as "alkalinity" in practical applications. The parameter C.I. used herein is intended to maintain a generality in order to include the case where the specified pH is below that of the natural H_2O/CO_2 system as well. In that case, C.I. represents the Cl^- ion, i.e. addition of HCl into the solution with a negative value.

If an ideal solution is assumed, all activity coefficients in Equation (65) reduce to unity, and the solution can be readily obtained. For the case of non-ideal solutions, the coefficient matrix ([A]) contains the activity coefficients, which are functions of the unknown concentrations. Therefore, an iterative calculation scheme is necessary, where a first guess (e.g., the solution speciation with ideal solution assumption) is used to obtain the activity coefficients and set up the coefficient matrix. The solution speciation and the parameter "C.I." is then obtained by further iterations.

$$\begin{bmatrix} 1 & 0 & 0 & 0 & 0 & 0 & 0 & 0 & 0 & 0 \\ 0 & 0 & \gamma_{H^+} & 0 & 0 & 0 & 0 & 0 & 0 & 0 \\ 1 & -\gamma_{CO_2}K_{H,CO_2}e^{\left(\int_{P_{ws}}^{P}\frac{\bar{V}_{m,CO_2}}{RT}dP\right)} & 0 & 0 & 0 & 0 & 0 & 0 & 0 & 0 \\ 0 & -a_{H_2O}\gamma_{CO_2}K_{hyd} & 0 & \gamma_{H_2CO_3} & 0 & 0 & 0 & 0 & 0 & 0 \\ 0 & 0 & 0 & -\gamma_{H_2CO_3}K_{ca} & \gamma_{HCO_3^-}10^{-pH} & 0 & 0 & 0 & 0 & 0 \\ 0 & 0 & 0 & 0 & -\gamma_{HCO_3^-}K_{bi} & \gamma_{CO_3^{2-}}10^{-pH} & 0 & 0 & 0 & 0 \\ 0 & 0 & 0 & 0 & 0 & 0 & \gamma_{OH^-}10^{-pH} & 0 & 0 & 0 \\ 0 & 0 & 1 & 0 & -1 & -2 & -1 & -1 & 1 & 0 \\ 0 & 0 & 0 & 0 & 0 & 0 & 0 & 1 & 0 & 0 \\ 0 & 0 & 0 & 0 & 0 & 0 & 0 & 0 & 1 & -1 \end{bmatrix} \cdot \begin{bmatrix} f_{CO_2} \\ c_{CO_{2(aq)}} \\ c_{H^+_{(aq)}} \\ c_{H_2CO_{3(aq)}} \\ c_{HCO_{3(aq)}^-} \\ c_{CO_{3(aq)}^{2-}} \\ c_{OH^-_{(aq)}} \\ c_{Cl^-_{(aq)}} \\ c_{Na^+_{(aq)}} \\ C.I. \end{bmatrix} = \begin{bmatrix} p_{CO_2}\phi_{CO_2} \\ 10^{-pH} \\ 0 \\ 0 \\ 0 \\ 0 \\ a_{H_2O}K_w \\ 0 \\ c_{NaCl_{(aq)}} \\ c_{NaCl_{(aq)}} \end{bmatrix} \qquad (65)$$

An example of the solution speciation and the activity coefficients from such calculations are shown in Fig. 3. Fig. 3A demonstrates the speciation of the carbonate species at 10 °C for CO_2 partial pressures of 1 and 15 bar. At 1 bar CO_2, the solution speciation for all species show a nearly linear trend with pH, suggesting that the effect of non-idealities is rather small. That is also seen on the calculated activity coefficients in Fig. 3B, where the obtained values show only a small variation with pH. On the other hand, at 15 bar CO_2, the effect of non-ideal solution becomes significant at pH values about 6. That effect is readily observed by the non-linear behavior in Fig. 3A. At the same time, the calculated activity coefficients shown in Fig. 3B demonstrate a radical change in the same pH range. It should be noted that the main cause of the non-ideal behavior in the present discussion is the Na^+ ions present in the solution as represented by the calculated charge imbalance (C.I.) in
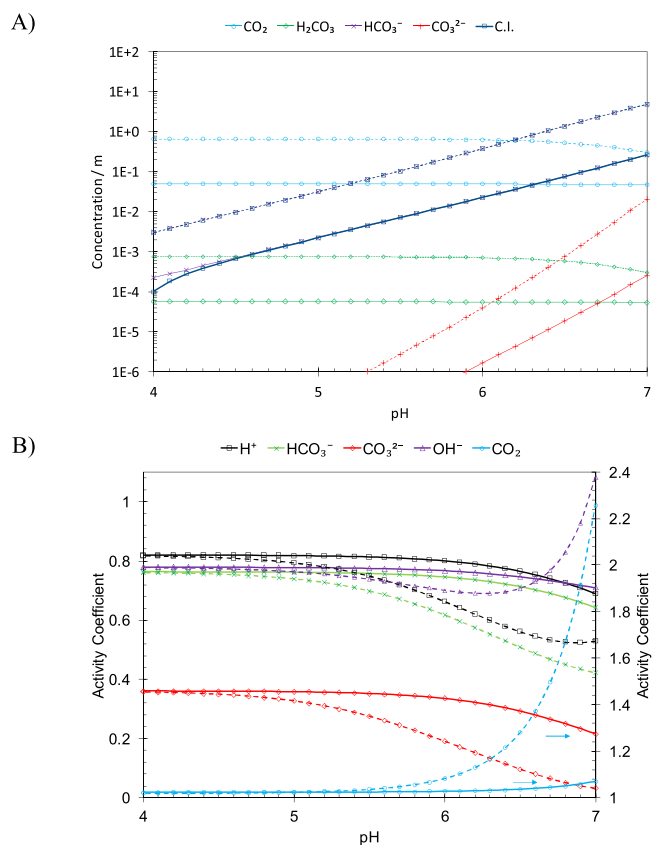
A)

B)

Fig. 3. The water chemistry calculation at 10 °C and 0.1 M NaCl at pCO$_2$ of 1 bar (solid lines) and 15 bar (dashed lines). (A) The calculated concentration of carbonate species and the charge imbalance (C.I.) as a function of pH. (B) The calculated activity coefficients as a function of pH on both horizontal axes.

Fig. 3A. In these conditions, this parameter can be associated with the concentration of NaOH or NaHCO$_3$ required to reach each specific pH.

As shown in Fig. 3B, the effect of non-idealities is not the same for all species; in some cases, even a trend reversal was observed. That is one of the main properties unique to the Pitzer's specific interaction model, and it is not properly reflected in more simplistic approaches like the Davies' equation, based on the initial Debye–Hückel theory. Additionally, such simplistic approaches suggest that the neutral species are not affected significantly by the non-ideal solution, while the calculation of the specific interactions showed that in the present case the activity coefficient of the dissolved CO$_2$ is increased by about two-folds in the pH range considered here.

The solution speciation and activity coefficient calculations are further verified as shown in Figs. 4 to 6. Fig. 4 shows the calculated pH at various partial pressures of CO$_2$ up to 60 bar. At such conditions, a reasonable agreement with the experimentally measured values of Meyssami et al. [66] was obtained, while at elevated pressures slight deviations are observed.

The performance of the non-ideal water chemistry calculations is further examined in the case of solutions containing a significant amount of additional NaCl. Fig. 5 shows the variation in pH as a function of pCO$_2$ in the solutions containing 0.5 M NaCl, at 26 °C, 50 °C, and 74 °C. The experimental data was taken from a study by Crolet and Bonis [67], and found to reasonably agree with the calculated values. The increasing trend of pH with increasing temperatures corresponds to increasing values of CO$_2$ Henry's constant (reduced solubility i.e. de-gassing) as well as increased dissociation equilibrium constants.

The effect of NaCl concentration is further examined in Fig. 6. While at low NaCl concentrations the solution pH was predicted with a fairly good accuracy, at higher salt concentrations the agreement is declined,
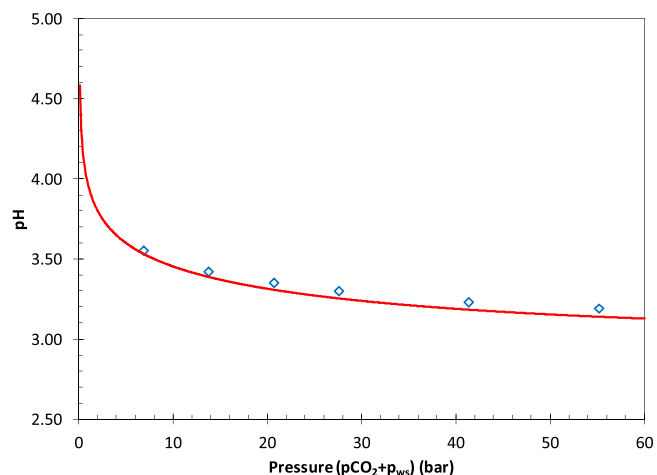

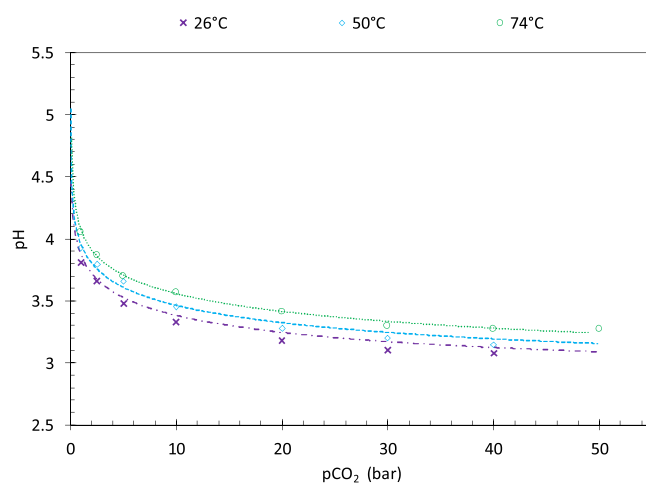**Fig. 4.** The comparison of the calculated solution pH under pure CO$_2$ atmosphere with the experimental data.

Fig. 5. The change in pH as a function of pCO$_2$ for a 0.5 M NaCl solution at 26 °C (purple × marks), 50 °C (blue diamonds), and 74 °C (green circles). The lines represent the calculated values, and the points are the experimental data taken from Crolet and Bonis [67]. (For interpretation of the references to colour in this figure legend, the reader is referred to the web version of this article.)
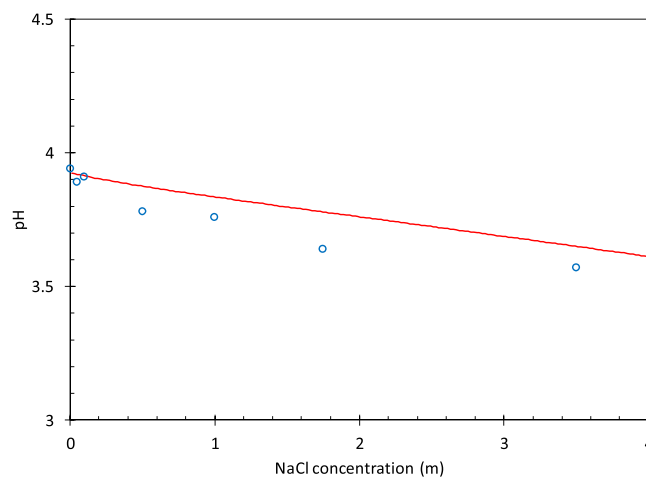

Fig. 6. The effect of NaCl concentration on the solution pH, at 25 °C, 1 bar CO$_2$. The solid line shows the calculated values, and the open circles show the experimental data taken from Crolet and Bonis [67].

e.g. at 3.5 M NaCl the predicted solution pH was about 0.1 pH units higher that the values reported experimentally [67]. Nonetheless, the predicted values do reflect the observed trend of pH and can be considered a significant improvement as compared to the case where the effect of non-idealities is ignored (pH at infinite dilution).

3.2. Effect of pCO_2 and pH on polarization behavior of the system

The polarization behavior in CO_2-saturated mildly acidic solutions was experimentally investigated on 316 L stainless steel and then on API 5 L X65 mild steel surfaces. The experiments were done in the pH range of 4–6 at CO_2 partial pressures from 1 to 15 bar. Based on the findings reported in our earlier studies [35–38], the present experiments were conducted mostly at 10 °C, in order to properly investigate the charge transfer mechanisms of the electrochemical reactions. The effect of temperature is addressed in a separate set of experiments, as discussed in more detail in the following sections.

The cathodic polarization curves obtained on the 316 L stainless steel surface are shown in Fig. 7. The polarization curves reported here all consist of a linearly increasing currents in low current density range, followed by the mass transfer limiting current, and a secondary linearly increasing current range at more negative potentials, associated with the reduction of water. Nevertheless, at pH 6, these characteristic behaviors are not as easily distinguishable due to the smaller "gap" between the H^+ reduction line and the water reduction line.

The first linear section of the polarization curve in low current density range is of particular interest in the present discussion, as it represents the charge transfer controlled cathodic current density, governing the corrosion current. The reported polarization curves for increasing pCO_2 values clearly show that, at a given pH, the cathodic currents in that range are insensitive to pCO_2. Considering the hypothesis presented earlier in the text, this observation indicates that H_2CO_3 is not a significant electro-active species and that the cathodic currents are only the result of H^+ reduction. Moreover, the results obtained at pH 6 and 15 bar CO_2, where the concentration of H_2CO_3 is 700 times higher than that of H^+ (see Fig. 3A), suggest that the H^+ reduction reaction is still the dominating cathodic reaction. This observation is found to agree well with those reported in earlier studies [33,36], suggesting that H_2CO_3 is not directly reduced on the stainless steel surface.

The limiting current densities are, on the other hand, significantly influenced by pCO_2, as expected. The presence of H_2CO_3 is known to increase the limiting current via two processes:

- H_2CO_3 as a weak acid with a relatively high equilibrium constant ($pK_a = 3.5$) and fast kinetics of dissociation ($k = 10^8$ s^{-1}), is an effective buffer. H_2CO_3 readily dissociates as the surface pH is increased in limiting current range of potentials, in order to maintain the chemical equilibrium. The dissociation reaction acts as an additional source of H^+ ions inside the boundary layer, and therefore results in increased limiting current densities.
- H_2CO_3 is also involved in the CO_2 hydration equilibrium. In that sense, the concentration of H_2CO_3 itself is also buffered by the dissolved CO_2 hydration reaction. Unlike H_2CO_3 dissociation, the dissolved CO_2 hydration reaction is limited by slow reaction kinetics.

The linear range of current densities observed at potentials more negative than those where the limiting currents are seen, are associated with the water reduction reaction, and show some variation with pCO_2. As is apparent from Fig. 7, this effect is more pronounced as the bulk pH is increased. Similar behavior was also reported previously in CO_2-saturated solutions as well as in solutions containing acetic acid [27,31].
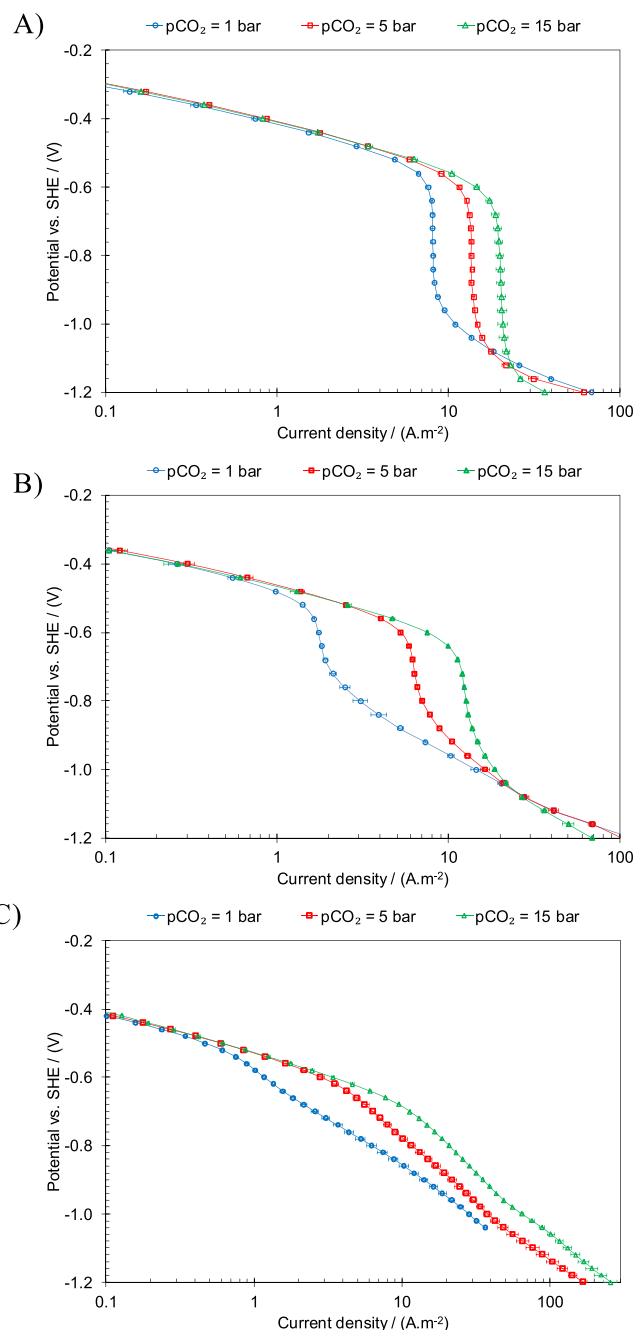
Fig. 7. The steady state cathodic polarization curves obtained on 316L stainless steel at 10 °C, 0.1 M NaCl, 4.4 m s^{-1} flow velocity, at pCO_2 of 1, 5, and 15 bar. (A) pH 4. (B) pH 5. (C) pH 6. The error bars show the standard deviation for at least three repeated experiments.

That can be associated with secondary effects related to $CO_{2(aq)}$ or other carbonate species interacting with the surface (e.g., via adsorption) and/or to the extreme surface pH values that are reached at such negative potentials. However, the exact mechanism behind this behavior is not clearly understood.

The polarization behavior of the API 5L X65 mild steel in CO_2-saturated solutions in the pH range from 4–6 and pCO_2 from 1 to 15 bar is shown alongside with the simulated polarization curves in Fig. 8. At pH 4, the cathodic polarization curves show the charge transfer controlled
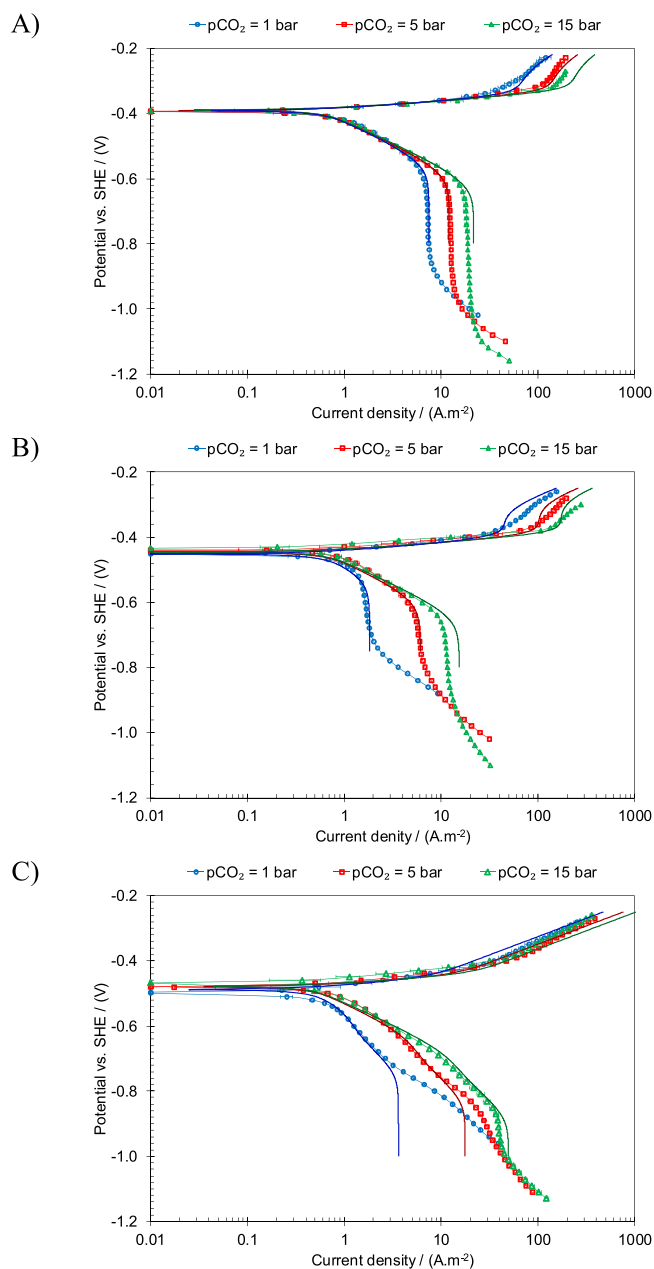
A)

B)

C)

Fig. 8. The comparison of the simulated (solid lines) and the experimental (points with dashed lines) polarization curves obtained on API 5L X65 mild steel at 10 °C, 0.1 M NaCl, 4.4 m s^{-1} flow velocity, at pCO$_2$ of 1, 5, and 15 bar. (A) pH 4. (B) pH 5. (C) pH 6. The error bars show the standard deviation of at least three repeated experiments.

Fig. 9. The illustration of the calculated surface activity of CO_2, H_2CO_3, and HCO_3^- versus the calculated surface pH, on primary vertical axis, and the current density on the secondary vertical axis (as a function of surface pH). Conditions: pH 6, 5 bar CO_2, 10 °C, 4.4 m s^{-1} TCFC flow.

transition range, which is expected to be followed by another linear range of current densities observed in the pre-passivation range [38,68]. Similar behavior was reported previously for iron dissolution during mild steel corrosion in CO_2-saturated solutions [38]. In the results reported here, the electrochemical response in the active dissolution range was insensitive to pCO$_2$, while a significant influence of pCO$_2$ on the magnitude of the current maximum in the transition range was observed. The pre-passivation range was not observed clearly in the experimental data obtained at this condition due to practical measurement limitations at those higher current densities. The observed behavior of the anodic polarization curve was in reasonable agreement with that reported previously [31,38].

The polarization data obtained at pH 5 (Fig. 8B) were found to be in general agreement with those at pH 4 (Fig. 8A) except at 1 bar CO_2. In this condition, the cathodic currents were to some degree under mass transfer influence, which resulted in an increase of the surface pH in the vicinity of OCP. These changes in the surface pH at and above the OCP lead to small deviations of anodic currents in the active dissolution range from the expected behavior. The charge transfer controlled cathodic currents observed at 5 bar and 15 bar CO_2 did not show any influence that could be associated with the direct reduction of H_2CO_3. The significant influence of pCO$_2$ on the anodic current maximum of the transition range was observed at pH 5, similar to that seen at pH 4.

The simulated polarization curves were found to agree well with the experimental data at both pH 4 and pH 5 as shown in Fig. 8. The model was found to be able to capture all mechanistic features of this electrochemical system. The cathodic polarization curves, including the limiting current and charge transfer controlled range, were successfully predicted without considering the direct reduction of H_2CO_3. This agreement is a further verification of the new mechanistic arguments about the mechanism of cathodic currents. At the same time, the anodic dissolution in the active range as well as the transition and the pre-passivation ranges, including their dependence on pCO$_2$, was predicted with a fairly reasonable accuracy. Some deviations were expected due to the simplified approach used to quantify such a complex reaction. This extends the range of validity of the incorporated model of iron dissolution to pCO$_2$ as high as 15 bar.

At pH 6, the polarization data showed somewhat a different characteristic behavior, as shown in Fig. 8C. At pH 4 and pH 5, a single

cathodic currents over an extended range as seen in Fig. 8A. Increasing the pCO$_2$ from 1 to 15 bar did not result in any appreciable change in the current densities across that range. This was found to be in agreement with results observed on the stainless steel surface shown in Fig. 7 and those reported earlier [35–37].

The anodic polarization curves at pH 4 (Fig. 8A) demonstrate a linearly increasing range at the potentials just above the OCP, which is associated with the active dissolution range of the iron oxidation reaction. At even higher potentials, an abrupt increase of the Tafel slope was observed. This range of current densities is categorized as the
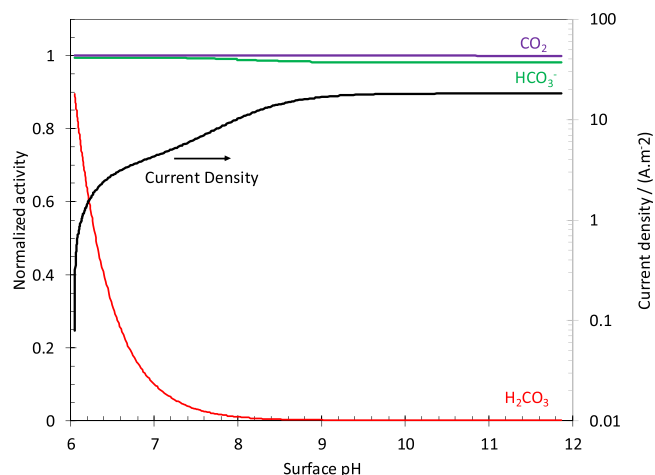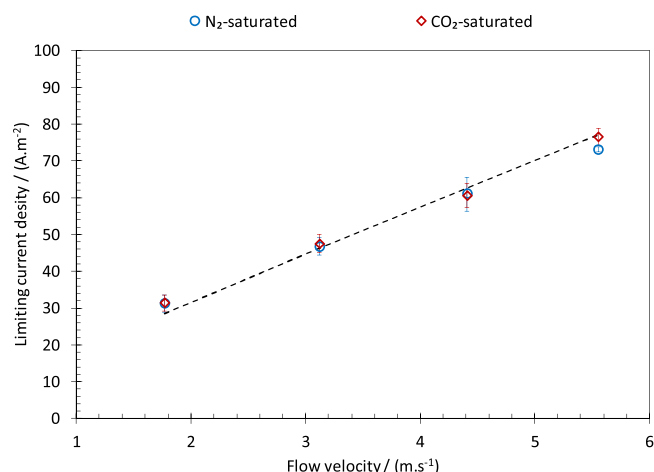
Fig. 10. The comparison of the calculated limiting current density (line) at pH 3, 10 °C, 0.1 M NaCl, $pCO_2 = 0$, with experimental data obtained at similar conditions (blue circles) and in solutions with $pCO_2 = 1$ bar (red diamonds). (For interpretation of the references to colour in this figure legend, the reader is referred to the web version of this article.)

Fig. 11. The experimental steady state polarization curves (points with dashed lines) obtained at pH 4, 5 bar pCO_2, 4.4 m s^{-1} TCFC flow, and 0.1 M NaCl on a API 5L X65 mild steel at various temperatures. The solid lines show the calculated polarization curves. The error bars show the standard deviation of at least three repeated experiments.

limiting current was observed at about −0.6 V (vs. SHE). The magnitude of the first limiting current observed at pH 6 was found to be close to the limiting current at pH 4 and pH 5. Considering the high pCO$_2$ (in the case of 5 and 15 bar) and the high flow velocity, pH effect on the limiting current density is expected to be small. Therefore, the first limiting current observed at pH 6 can be associated with the same process – H$^+$ reduction buffered by the H$_2$CO$_3$ dissociation reaction.

At 1 bar CO$_2$, the cathodic current range is greatly influenced by the limiting current. However, at 5 bar and 15 bar CO$_2$ the linear range of cathodic currents just below the OCP and before the first limiting current indicates a charge transfer controlled range. This range of cathodic currents was also found to be insensitive to pCO_2, what is expected when H$_2$CO$_3$ is not electrochemically active. This observation is of importance since it significantly extends the range of validity of the previous arguments on the electrochemical activity of H$_2$CO$_3$ on mild steel surface and is similar to what was found on stainless steel.

Additionally, at pH 6 a second limiting current at about −0.9 V (vs. SHE) was observed. The cathodic currents observed below the first limiting current are likely associated with the presence of HCO$_3$$^-$. This behavior provides an opportunity to evaluate the role of HCO$_3$$^-$ in CO$_2$ corrosion in near neutral pH values. In the mechanistic studies of corrosion in the presence of weak acids it is common to readily associate the observation of a second limiting current with the direct reduction of a weak acid. For example as was done in the cases of aqueous H$_2$S [69–71] and sulfurous acid [72]. That can be readily shown not to be the case for HCO$_3$- based on the magnitude of the limiting current, without getting into a detailed quantitative discussion at this point. Considering the rather high concentration of HCO$_3$$^-$ (about 0.1 M) at pH 6 and 15 bar CO$_2$, with some simple mathematical estimations one would expect the mass transfer limiting current for HCO$_3$- direct reduction to be one to two order of magnitude higher than what is observed in Fig. 8C. That suggests the appearance of this secondary wave is not due to an additional HCO$_3$$^-$ reduction reaction, but rather is caused by kinetically controlled chemical buffering of H$^+$ by HCO$_3$$^-$ dissociation.

In light of the results obtained from the mathematical model, the experimental data obtained at pH 6 can be discussed in a more quantitatively accurate fashion. As shown in Fig. 8, the model successfully predicts the seemingly different governing mechanisms at pH 6;
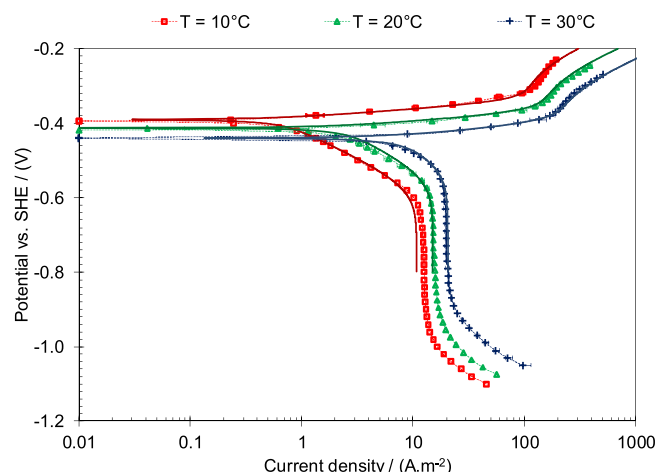
including the "double wave" in cathodic currents. Yet, in the present model, the only electroactive cathodic species is the H$^+$. The underlying mechanism can be deducted by analysis of surface concentration of the carbonate species. Fig. 9 illustrates the calculated surface activity of the involved carbonate species (normalized by using bulk activities) as a function of the calculated surface pH, on the primary axis. The corresponding current response is demonstrated on the secondary axis. The simulation results show that as the first limiting current is approached, the surface pH gradually increases from the bulk value, which is at the same time accompanied by the decrease of H$_2$CO$_3$ surface activity due to its chemical dissociation. This trend is continued until the first limiting current is reached (at ∼4 A m^{-2}), where the surface H$_2$CO$_3$ activity approaches zero. The increase in current density after the first limiting current is associated with further increase of surface pH that favors the dissociation of HCO$_3$$^-$ as seen by its depleting surface activity. Ultimately, where the rate of HCO$_3$- dissociation reaches its maximum (the activity plateau), the second limiting current is observed. Hence, the predicted secondary limiting current is a result of the homogeneous HCO$_3$- dissociation that is favored at the
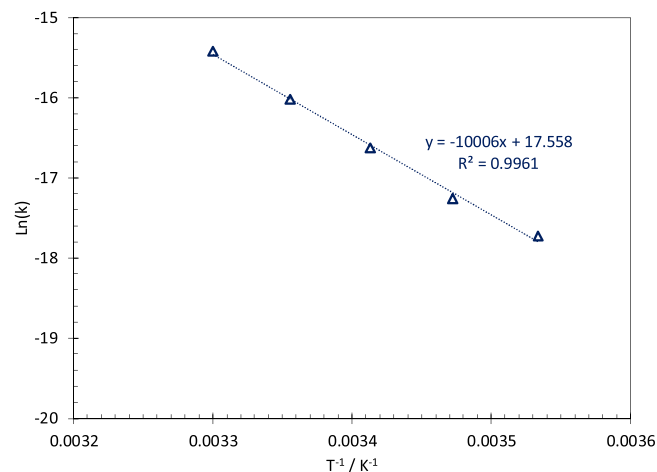

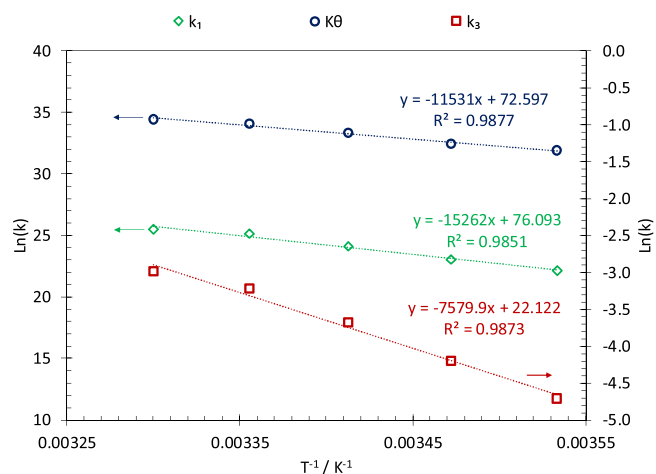**Fig. 12.** The Arrhenius plot for the temperature dependence of the H$^+$ reduction kinetic rate constant.

Fig. 13. The Arrhenius plot for the temperature dependence of the kinetic rate constant of the components of the iron dissolution reaction.

Fig. 14. The Arrhenius plot for the kinetic rate constant of the HCO_3^- dissociation.

high surface pH in such conditions.

As shown in Fig. 9, while the surface H^+ and H_2CO_3 activities are dramatically decreased at the limiting current range, the activities of CO_2 and HCO_3^- are only slightly changed, which indicates the slow kinetics of their corresponding chemical reactions. The buffering ability of H_2CO_3 and that of HCO_3^- may be distinguished in this regard. H_2CO_3 can be considered a strong buffer in the sense that its equilibrium and kinetics allow this species to readily dissociate as the surface pH is increased; this is the same behavior as observed for the case of carboxylic acids [27,28]. As discussed in the introduction section, such behavior makes the limiting currents of these strong buffers to be identical whether the weak acid is directly reduced or not, and hence the mechanism of the reaction had to be discussed only based on the response of the system at the charge transfer range. On the other hand, HCO_3^- can be regarded as a weak buffer, due to its low pK_a and slow reaction kinetics that hinders its dissociation under limiting current conditions. This distinct behavior provides a simple and definitive means to show that the contribution of HCO_3^- to the cathodic current is through its homogeneous chemical dissociation (buffering effect). Noting that in the case of direct reduction reactions the limiting current is defined by mass transfer of the active species. As shown in Fig. 9, the observed second limiting current is the result of consumption of only ~ 5% of the HCO_3^- at the surface. In that sense, if HCO_3^- was directly reduced, the limiting current was expected to be about 20 times higher than that observed experimentally.

The second limiting current becomes less obvious at elevated CO_2 partial pressures, and is only observed as a change in the apparent slope of the cathodic currents at 15 bar CO_2. That behavior was also predicted by the model via the buffering effect of HCO_3^-. It should be noted that the current density range in between the two limiting currents are no longer under pure charge transfer control but controlled by the surface concentration of H^+ that is provided by the slow HCO_3- dissociation reaction. Therefore, this range of current densities are pCO_2 dependent through the pCO_2 dependence of HCO_3^- concentration, a behavior that is seen in Fig. 8.

The discussion in this section indicates that in acidic CO_2 corrosion neither H_2CO_3 nor HCO_3^- are directly reduced at the metal surface to any significant extent, and the higher corrosion rates in CO_2-saturated environments are the results of the complex set of homogeneous chemical reactions associated with the H_2O/CO_2 system at the vicinity of the metal surface. That also highlights the capability and the necessity
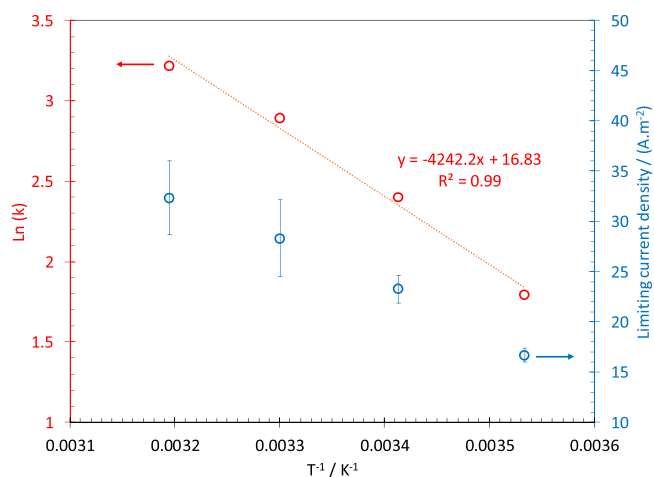
of the comprehensive mathematical models for incorporating the surface chemistry in corrosion rate calculations.

The anodic polarization at pH 6 was also found to behave differently from what was observed at pH 4 and 5. The most significant aspect is the absence of the transition range and its corresponding current maximum. Beside the slight deviation at 1 bar CO_2, caused by the previously discussed change in surface pH that is a result of mass transfer limited cathodic current densities, the pCO_2 dependence observed at pH 6 was somewhat lower than that observed at pH 4 and 5. That includes the current densities associated with the pre-passivation range at higher potentials, identified by the higher Tafel slope (~ 120 mV). These observations suggest a rather significant change of the iron dissolution mechanism at pH 6. Nonetheless, the simulated results were found to be able to capture this behavior. The results from the model at pH 6 suggests that, unlike what is seen in lower pH, the active dissolution range is no longer observed. The observed anodic currents were dominated by the reaction associated with the pre-passivation range (at both low Tafel slope and high Tafel slope ranges). The different Tafel slopes observed at lower and higher current densities are the result of the dependence of this reaction on the surface coverage of the intermediate species (θ). Where at low coverages, when θ is potential dependent as described by Equation (49), a lower Tafel slope is observed. As θ approaches 1 and no longer increases with increasing potentials, the second range of current densities, with an increased Tafel slope, is observed. Considering the experimental errors, the simulated behavior of the anodic current was in reasonable agreement with the experimental data, however, the pCO_2 dependence as well as the Tafel slope appear to be slightly lower than that seen at lower pH values.

3.3. Effect of flow

The most obvious way that flow affects CO_2 corrosion is by changing the magnitude of the limiting current density. In many practical scenarios, especially those at higher temperatures when the charge transfer processes are fast, the corrosion rate is under mass transfer control, and is defined by the cathodic limiting current density. As discussed above, the mass transfer of H^+ and H_2CO_3 from the bulk are major components of limiting current, in addition to the effect of CO_2 hydration, H_2CO_3 and HCO_3^- dissociation reactions in the vicinity of the metal surface.
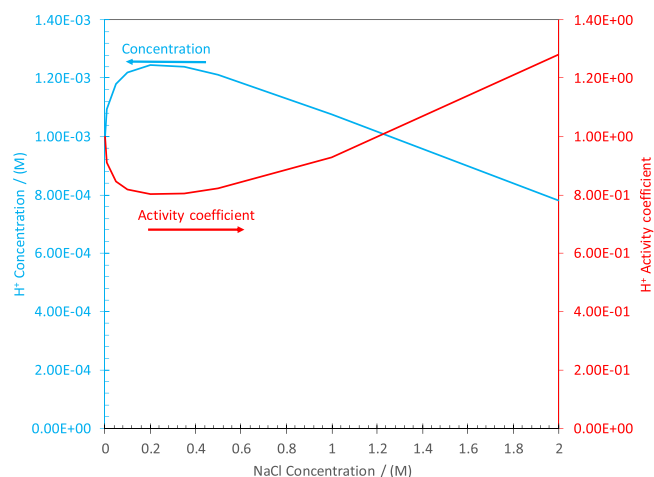
Fig. 15. Concentration (primary vertical axis) and activity coefficient (secondary vertical axis) of hydrogen ion as a function of NaCl concentration at a constant pH of 3 and 10 °C as calculated by water chemistry model.

In the present model, the mass transfer in turbulent flow regimes is accounted for in terms of eddy diffusivity, as seen in Equation (56). This approach remains valid for most fully developed turbulent flow regimes, including the thin channel flow used in the current experiments as well as pipe flow in the industrial applications. In order to examine the performance of this approach for determining the limiting currents, a series of experiments with flow velocity as a variable was considered. The experiments were conducted at pH 3 in N_2-saturated and CO_2-saturated solutions, where the limiting currents could be observed clearly under atmospheric pressure. Fig. 10 demonstrates the comparison of the limiting current densities predicted by the model with those obtained experimentally. At pH 3, considering the high concentration of H^+ and the large flow velocity, no significant effect from the presence of CO_2 was observed due to the overwhelmingly high mass transfer of H^+ from the bulk solution overshadowing the buffering reactions associated with the presence of CO_2 species. That is the ideal condition when one attempts to single out the effect of mass transfer for close examination, similar to the objectives in this section. Overall, the agreement of the model with the measured limiting current densities was found to be satisfactory, demonstrating the accuracy of the model in calculating the flow effect.
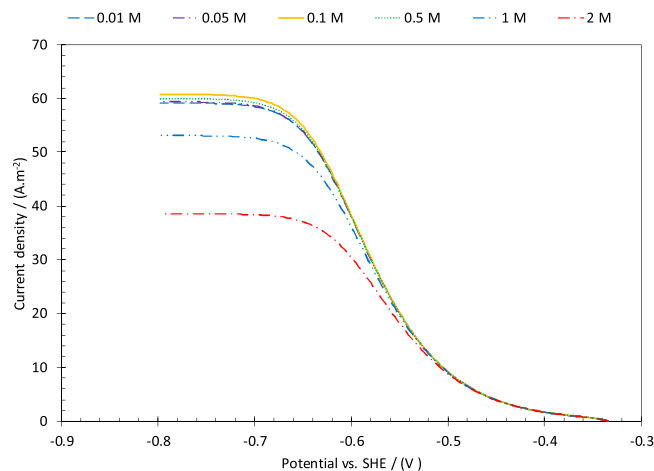

Fig. 16. The predicted current/potential response at pH 3, 10 °C, 4.4 m s^{-1} flow velocity and various NaCl concentrations.

3.4. Effect of temperature

Temperature has a significant known effect on almost all aspects of CO_2 corrosion. As shown in Fig. 11, increasing temperature results in increased rate of charge transfer processes and the limiting current. The effect of temperature in the latter case is, for the most part, on the kinetics and equilibria of the CO_2/H_2O system. Some less significant effects resulting from the change in the physical properties of water (e.g., water density and viscosity) and the diffusivity of the species are also expected. These effects are incorporated in the present calculations, and as shown in Fig. 11 the predicted limiting currents are found to be in reasonable agreement with the experimental data.

The two electrochemical reactions in the present discussion are the H^+ reduction and iron oxidation in the active dissolution range, occurring at the vicinity of the corrosion potential. The temperature dependence of these two reactions can be discussed best at the conditions where the cathodic currents are clearly observed, and the anodic currents show the active dissolution in over rather extended range. The polarization data obtained at pH 4 and 5 bar CO_2 and 10 °C showed that such considerations are reasonably satisfied at this condition, and hence it was selected as the baseline condition for further investigation of the temperature effect. The results shown in Fig. 11 suggest that both charge transfer reactions (anodic and cathodic) have a rather a high temperature dependence. At about 30 °C their rate is already so fast that the limiting effect of mass transfer becomes significant, even at the corrosion potential, distorting the shape of the lines for both the cathodic and anodic currents. Therefore, the temperature dependence of these electrochemical reactions can only be discussed properly in the lower temperature range.

The temperature dependence of the charge transfer reactions were obtained by using Arrhenius plots as shown in Fig. 12 and Fig. 13. Fig. 12 shows the temperature dependence of the H^+ reduction reaction, where the natural log of the apparent reaction rate constant, as obtained by the best fit of the model to the averaged data of Fig. 11, is plotted as a function of $1/T$. The slope of the trend line is equal to $-E_a/R$. Considering these results, the apparent activation energy of H^+ reduction was found to be 83.2 kJ. The activation energy obtained here is in a similar range to that obtained in our earlier study (about 20% variation) [35]. However, it differs significantly from the earlier reported values at about 30 kJ [19,24,73]. The substantial difference could be the result of underestimated activation energy in the earlier studies due to mass transfer interference at higher temperatures.

The temperature dependence of the iron dissolution reaction was obtained in a similar fashion. As discussed earlier, the iron dissolution was expressed as a combination of four reactions [35]. Fig. 13 shows the temperature dependence of k_1, k_3, and K_θ, for the reactions in the active dissolution range, pre-passivation range and the equilibrium constant of its associated intermediate species, respectively. Similar to the cathodic reaction, the iron dissolution reaction also shows a rather significant temperature dependence, especially in the active dissolution range. The activation energies for k_1, k_3, and K_θ were estimated to be 126.8 kJ, 63.0 kJ, and 95.8 kJ, respectively.

It should be noted that the reaction in the active dissolution range with rate constant of k_2 is not observed at this pH and pCO_2 range. As discussed previously [35], that reaction is only significant in a narrow range of condition at pH values somewhere between 5 and 6. As it becomes rate determining at pH 6, it diminishes the currents in whole active dissolution range (see Fig. 8). In such conditions the anodic current is a result of one reaction sequence, from OCP all the way up to pre-passivation range. Its transitional nature and a narrow range of conditions where it is observed, makes the quantitative determination of its rate and temperature dependence difficult. On the other hand, for the same reason its contribution to the accuracy of corrosion rate prediction in CO_2 systems is relatively small and it was here established that the temperature dependence of this parameter has no significant influence on the practical performance of the model. An example of the
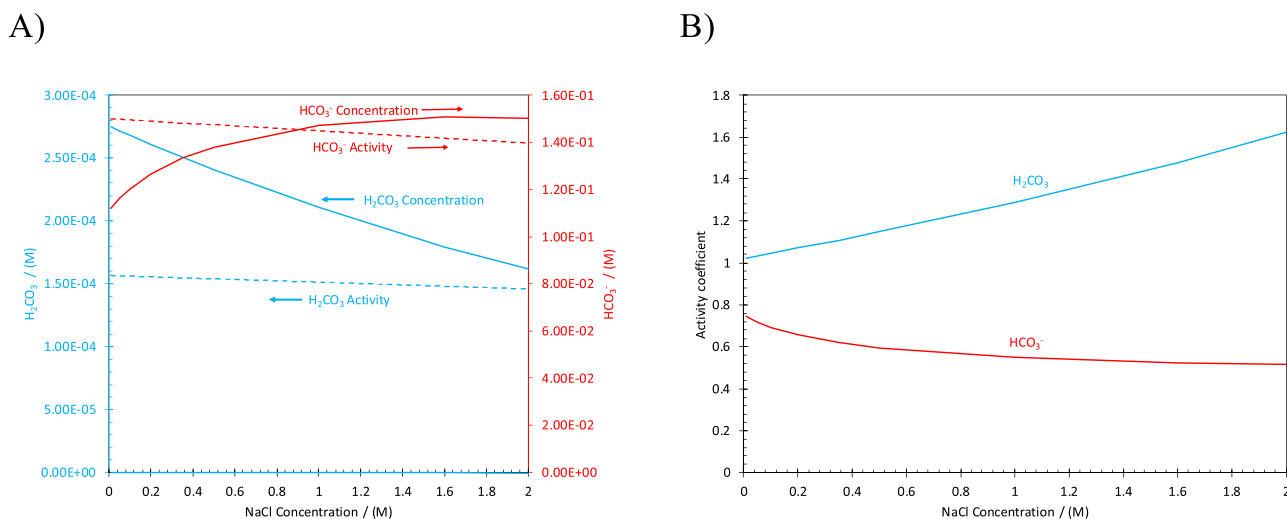
A)

B)

Fig. 17. Effect of NaCl concentration on the concentration, activity and activity coefficient of H_2CO_3 and HCO_3^- at pH 6, 5 bar CO_2, and 10 °C as calculated by the water chemistry model. A: Effect of NaCl concentration on concentration (solid lines) and activities (dashed lines) of H_2CO_3 (blue lines) and HCO_3^- (red lines). B: Effect of NaCl concentration on activity coefficient of H_2CO_3 (blue line) and HCO_3^- (red line). (For interpretation of the references to colour in this figure legend, the reader is referred to the web version of this article.)
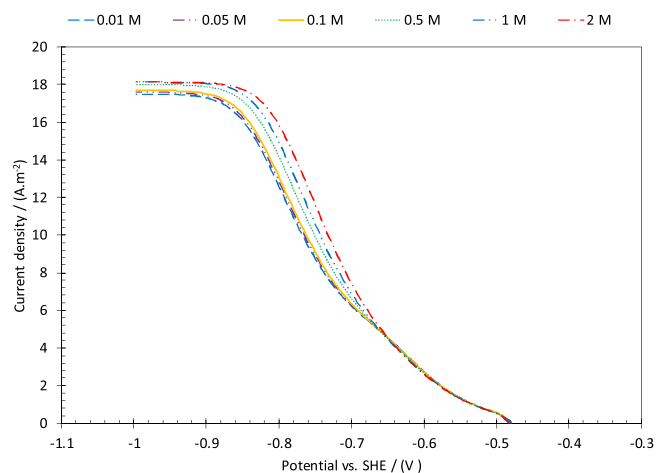

Fig. 18. The predicted current/potential response at pH 6, 5 bar CO_2, 10 °C, 4.4 m s^{-1} flow velocity and various NaCl concentrations.

estimated polarization curves shown in Fig. 11, confirms a good agreement between the experimental data and the calculations, by using the temperature dependencies determined as described above.

The temperature dependence of the kinetics of homogeneous chemical reactions are worthy of a further discussion. As noted above, the CO_2 corrosion involves a series of homogeneous chemical reactions with extremely high rate constants. The association of H_2CO_3, and HCO_3^- are examples of such reactions. In the present discussion the dissociation rate of H_2CO_3 and HCO_3^- and their temperature dependences are of particular interest. For the case of H_2CO_3, the reported rate of the backward reaction is of the order of 10^{10} (M^{-1} s^{-1}) and the equilibrium constant of the order of 10^{-3} (M), this suggests that the rate of H_2CO_3 dissociation reaction at room temperature is of the order of 10^7 (s^{-1}). With such a high kinetic rate constant this reaction is not expected to be rate limiting even at most extreme conditions encountered in CO_2 corrosion scenarios. Therefore, the temperature dependence of the rate of this reaction is not of any practical significance and can be treated as a constant value. On the other hand, for the case

of HCO_3^- dissociation, even though the association reaction is also known to be very fast, the equilibrium constant of the order of 10^{-10} (M) suggests that the dissociation reaction is rather slow at room temperature. This was observed in the polarization curves reported in Fig. 8, where the limiting current density associated with the buffering effect of HCO_3^- was limited by the kinetics of dissociation reaction.

In the present study, the rate constant of the HCO_3^- dissociation and its temperature dependence was estimated based on the second limiting current densities obtained at pH 6 and pCO$_2$ of 5 bar. Fig. 14 shows the limiting current densities at this range measured at temperatures from 10 °C to 40 °C, and corrected for the contribution of water reduction reaction, assuming a Tafel behavior. The measurements showed increased scattering with increased temperatures, as indicated by the larger error bars. The measured limiting currents do not have a simple relationship with the bicarbonate dissociation rate constant since they also include the effects of mass transfer of H^+, H_2CO_3, and HCO_3^-, in addition to effects associated with the CO_2 hydration and H_2CO_3 dissociation reactions. In order to obtain reasonably confident estimations, the rate constant of the HCO_3^- dissociation reaction was obtained based on the best fit of the model to the average values of the measured limiting currents. By doing so, all the abovementioned components of the limiting current are accounted for. The results obtained in this fashion are shown in the primary axes of Fig. 14, and the rate constant of HCO_3^- dissociation was expressed as shown in Table 5.

3.5. Effect on non-ideal behavior

There is no simple way to predict the effect of non-ideal behavior on the electrochemical response of the CO_2/H_2O system and corrosion rates. That arises from the different responses of the electrochemical reaction rates and mass transfer processes to non-idealities due to the opposing change in activity coefficient and concentration. While the chemical and electrochemical reactions are governed by the activity of the chemical species, the mass transfer process is governed by a mixture of activities and concentrations. For example, molecular diffusion is defined by chemical activity of the involved species while turbulent mixing and electromigration are governed by concentrations. The

Table 9

Corrosion rate data obtained from LPR measurements. The values in parentheses represent the corresponding standard deviation.

pH	pCO_2 (bar)	T (°C)	n	B	Polarization resistance (Ohms)	Solution resistance (Ohms)	Corrosion current density (A m^{-2})	Corrosion rate (mm year^{-1})
4	1	10	4	8.90E-03	8.74E+01 (1.54E+00)	1.02E+01 (5.66E-01)	5.78E-01 (1.09E-02)	6.71E-01 (1.27E-02)
4	5	10	6	8.90E-03	8.78E+01 (2.15E+01)	1.12E+01 (1.95E-15)	6.61E-01 (3.35E-01)	6.08E-01 (2.56E-02)
4	5	15	4	8.26E-03	5.69E+01 (3.19E+00)	1.02E+01 (2.65E-01)	8.89E-01 (6.26E-02)	1.03E+00 (7.26E-02)
4	5	20	7	8.58E-03	4.13E+01 (3.54E+00)	8.67E+00 (1.38E+00)	1.34E+00 (1.81E-01)	1.56E+00 (2.10E-01)
4	5	25	4	8.90E-03	2.49E+01 (2.56E+00)	8.23E+00 (3.30E-01)	2.74E+00 (4.71E-01)	3.18E+00 (5.46E-01)
4	5	30	4	1.12E-02	1.73E+01 (5.57E-01)	7.33E+00 (4.27E-01)	5.67E+00 (4.27E-01)	6.58E+00 (4.95E-01)
4	5	40	4	1.18E-02	1.06E+01 (3.62E-01)	6.34E+00 (3.77E-01)	1.43E+01 (2.24E+00)	1.66E+01 (2.60E+00)
4	15	10	6	8.90E-03	9.10E+01 (6.12E+00)	1.18E+01 (4.42E-01)	5.66E-01 (4.73E-02)	6.57E-01 (5.49E-02)
5	1	10	5	9.06E-03	1.05E+02 (3.18E+00)	1.14E+01 (6.20E-01)	5.04E-01 (4.29E-02)	5.85E-01 (4.98E-02)
5	5	10	6	8.90E-03	8.60E+01 (5.55E+00)	1.00E+01 (2.86E-01)	5.90E-01 (4.64E-02)	6.85E-01 (5.39E-02)
5	5	40	4	8.90E-03	1.65E+01 (3.37E-01)	6.05E+00 (1.73E-01)	4.28E+00 (2.08E-01)	4.96E+00 (2.41E-01)
5	15	10	6	8.90E-03	9.80E+01 (7.77E+00)	1.07E+01 (3.78E-01)	5.15E-01 (4.67E-02)	6.08E-01 (5.28E-02)
6	1	10	7	9.20E-03	1.54E+02 (3.00E+00)	1.00E+01 (5.45E-01)	3.57E-01 (1.01E-01)	4.15E-01 (1.17E-01)
6	5	10	6	8.90E-03	1.09E+02 (7.10E+00)	6.27E+00 (3.83E-01)	4.37E-01 (3.12E-02)	5.07E-01 (3.62E-02)
6	5	20	6	1.45E-02	6.09E+01 (2.19E+00)	4.85E+00 (3.08E-01)	1.30E+00 (5.09E-02)	1.51E+00 (5.90E-02)
6	5	30	8	1.50E-02	3.74E+01 (1.15E+00)	4.36E+00 (2.64E-01)	2.28E+00 (9.06E-02)	2.64E+00 (1.05E-01)
6	5	40	10	1.53E-02	2.40E+01 (8.26E-01)	3.96E+00 (2.07E-01)	3.85E+00 (1.64E-01)	4.46E+00 (1.91E-01)
6	15	10	6	8.90E-03	1.20E+02 (3.09E+00)	3.57E+00 (2.42E-01)	3.83E-01 (9.80E-03)	4.45E-01 (1.14E-02)
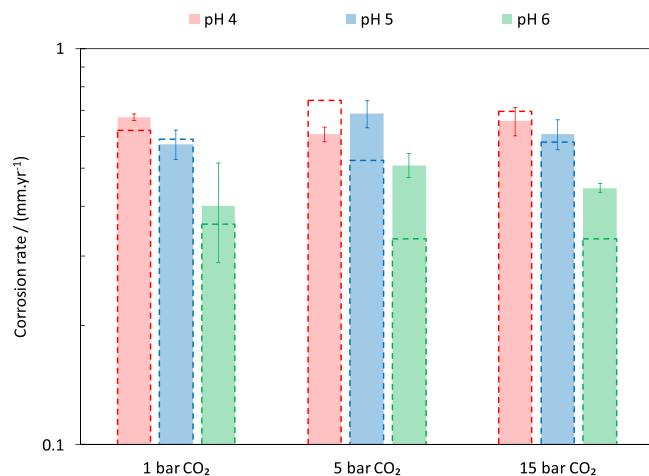
Fig. 19. The comparison of the estimated (dashed bars) and the measured corrosion rates (solid bars) at 10 °C, 4.4 m s^{-1} TCFC flow, and 0.1 M NaCl on a API 5L X65 mild steel.
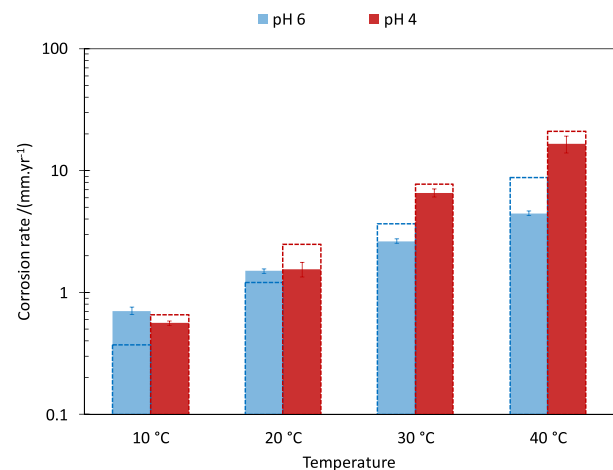
Fig. 20. The comparison of the estimated (dashed bars) and measured (solid bars) corrosion rates at 5 bar pCO_2, 4.4 m s^{-1} TCFC flow, and 0.1 M NaCl on a API 5L X65 mild steel at various temperatures, at pH 4 and pH 6.

proper prediction of the effect of non-idealities necessitates calculations that simultaneously account for various physiochemical processes alongside the local activity and concentration calculations, similar to the comprehensive mechanistic model developed in the present study.

The present model can be used to demonstrates the influence of the non-ideal solutions on the electrochemical response of the system. In particular, the cathodic currents are of more significance in this

discussion as they are influenced profoundly by the solution speciation. Fig. 15 shows the effect of NaCl concentration on the concentration and the activity coefficient of hydrogen ion, while the solution pH (hence, H$^+$ activity) was kept at constant value of 3. Increasing the NaCl concentration from the initial infinite dilute solution results in an increase in the concentration of H$^+$, which corresponds to decreasing activity coefficient from the unity. However, further increase of NaCl
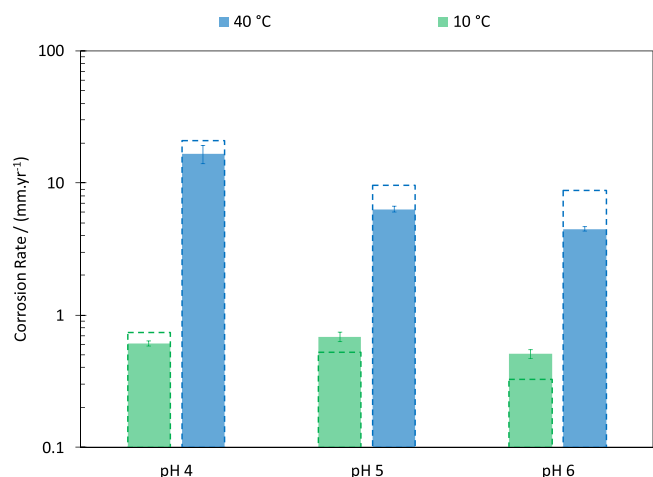
Fig. 21. The comparison of the estimated (dashed bars) and the measured (solid bars) corrosion rates at 10 °C and 40 °C, 4.4 m s^{-1} TCFC flow, 0.1 M NaCl, 5 bar pCO$_2$, and pH values from 4.0 to 6.0, on a API 5L X65 mild steel.
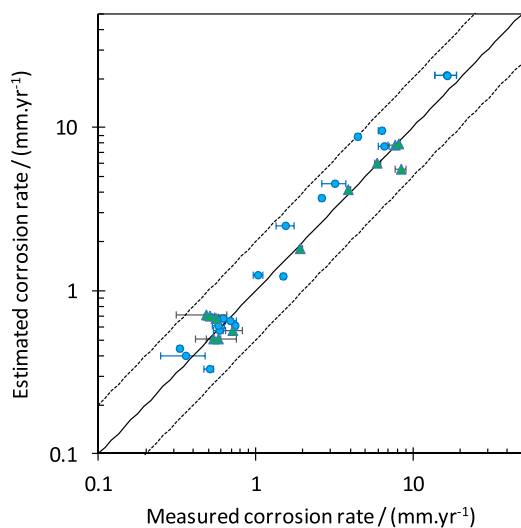

Fig. 22. Parity graph of the corrosion rate data and the estimated values at $0 < p$CO$_2 < 15$ bar, $4.0 < pH < 6.0$, 10 °C $< T < 40$ °C, TCFC flow at 4.4 m s^{-1} (blue circles) and 12.9 m s^{-1} (green triangles) from [35]. The dashed lines represent a two-folds error limit. (For interpretation of the references to colour in this figure legend, the reader is referred to the web version of this article.)

concentration results in a reversed trend, where a decrease in H$^+$ concentration is observed at higher NaCl concentrations, associated with the increasing activity coefficients, even to values above unity.

The predicted cathodic polarization curves corresponding to these conditions are shown in Fig. 16. The correlation between the H$^+$ concentration and the polarization behavior is clearly observed. By fixing the pH, the charge transfer controlled cathodic current densities remain unchanged since the driving force, activity of H$^+$, is kept constant. On the other hand, the magnitude of the mass transfer limiting current correlates directly with the concentration of H$^+$. The initial increase of NaCl resulting in the increased concentration, corresponds to increasing limiting current densities. As the NaCl concentration is increased further, the limiting current density gradually decreases. It is worthwhile to mention the trend of limiting current density presented in Fig. 16 is specific to the environmental conditions of the present discussion. For example, the relatively high flow velocities here make the turbulent mixing of H$^+$ the dominating process defining the magnitude of the limiting current density. At lower flow velocities, where the molecular

diffusion is dominating, the magnitude of limiting current is expected to follow the trend of the activity rather than concentration.

The effect of NaCl concentration on the cathodic polarization curves of CO$_2$/H$_2$O system can be discussed in the same fashion. Fig. 17 shows the effect of NaCl concentration on the concentration, activity, and activity coefficient of H$_2$CO$_3$ and HCO$_3^-$ ion at 5 bar CO$_2$ partial pressure, while the solution pH was maintained at 6. At such environmental conditions, the cathodic current densities after the first limiting current is significantly influenced by the solution speciation, due to the dominating role of homogeneous chemical reactions in defining the surface concentration of H$^+$. The limiting currents are also to the most part defined by kinetics of the homogenous chemical reaction: the first limiting current by kinetics of CO$_2$ hydration reaction, and the second limiting current by the kinetics of HCO$_3^-$ dissociation reaction. With activities as the driving force of these reactions, the limiting currents are expected to mostly follow the trend of this parameter, while some influence of the underlying mass transfer effect is also expected.

As shown in Fig. 17A, unlike activity coefficient and concentration, activity of the carbonate species are only slightly affected by NaCl concentration due to the chemical equilibrium constraint governing their values (considering that pH and pCO$_2$ are kept constant). Fig. 18 demonstrates the calculated cathodic polarization curves at pH 6, 5 bar CO$_2$ and increasing NaCl concentration. At such conditions no simple correlation between the behavior of polarization curves and concentration, activity or activity coefficient of the involved species can be identified. Here the current densities in the range between the two limiting currents are significantly affected by the non-ideal solution properties, while the magnitude of the limiting current densities themselves are less affected by increased NaCl concentration as compared to that seen in Fig. 16.

3.6. Corrosion rates

The calculated corrosion rates are compared with the experimental data obtained from LPR measurements. The experimental polarization resistance data (R_p) was first corrected for the solution resistance obtained from EIS measurements. The corresponding corrosion current were then calculated as shown below. Where A is the electrode surface area (m^2) and B values were estimated empirically based on the apparent Tafel slopes obtained from the polarization data corresponding to each condition as shown in Table 9.

$$i_{Corr} = \frac{B}{R_p/A}$$

Fig. 19 shows the results obtained at 10 °C corresponding to the polarization curves shown in Fig. 8. Over the range of conditions covered here the cathodic currents are, to the most part, under charge transfer control and the anodic currents are at the active dissolution range (with the exception of pH 6) at the vicinity of the corrosion current. At such conditions, neither the cathodic currents nor the anodic currents were expected to be significantly influenced by the partial pressure of CO$_2$. Hence, no significant dependence of corrosion rate on pCO$_2$ is expected, which is the behavior reflected both in the experimental data and the predicted values. Also, the experimental data and the predicted corrosion rates show no notable dependence on the solution pH at such conditions. That suggests the increased rate of iron dissolution with pH and the decreased rate of hydrogen reduction reaction are such that the net effect become almost independent of pH. Such behavior is not universal and expected to vary depending on the solution speciation and the environmental conditions. For example, if the corrosion potential is at the transition range or it is influence by cathodic limiting current a prominent pH dependence may be observed. Example of such behavior can be seen in the data obtained at elevated temperatures shown in Fig. 20 and Fig. 21.

The effect of temperature on corrosion rates and the model's prediction performance is shown in Fig. 20, for pH 4 and pH 6, at 5 bar

pCO$_2$. As expected, the increasing temperatures results in significantly higher corrosion rates. The estimated corrosion rates were found to agree reasonably well with those obtained experimentally, demonstrating the capabilities of the model in capturing the effect of temperature. Furthermore, the estimated corrosion rates at 5 bar pCO$_2$ for various pH values and two temperatures, 10 °C and 40 °C, are compared with the experimental data in Fig. 21.

In order to examine the overall performance of the model, the estimated corrosion rates are compared with the experimental data in the parity graph of Fig. 22, for the broad range of environmental condition: $0 < p$CO$_2 < 15$ bar, $4.0 <$ pH < 6.0, 10 °C $< T < 40$ °C, flow $= 4.4$ m s^{-1} and 12.9 m s^{-1}. The total of 32 datapoints in Fig. 22 includes those obtained in the present study as well as the data reported in our earlier publication [35], each representing a distinct condition within the range noted above. Almost all data points fall within a band denoting a factor of two-fold difference, with the average absolute deviation of 19.9% between the experimental and predicted values. The overall agreement demonstrates the ability of the model to calculate the corrosion rates reasonably well across a wide range of experimental conditions.

4. Conclusions

The electrochemical behavior of CO$_2$-saturated acidic solutions on API 5L X65 mild steel and 316L stainless steel was investigated experimentally and theoretically in the pH range of 4–6 and for CO$_2$ partial pressures from 1 to 15 bar. The theoretical investigation of the system was done based on a comprehensive mechanistic mathematical model that was coupled with a Pitzer-type specific interaction model, in order to account for the non-ideal behavior of the system. The results showed that:

- In the modern mechanistic understanding of CO$_2$ corrosion of mild steel, it is shown that the corrosion process is the results of only two electrochemical reactions, hydrogen ion reduction as the sole cathodic reaction and iron dissolution as the sole anodic reaction. The direct reduction of H$_2$CO$_3$ and HCO$_3^-$ that previously believed to be essential aspects of CO$_2$ corrosion in classic mechanistic view are shown to be insignificant in an extended range of conditions. The increased cathodic limiting currents were fully explained by the buffering effect of H$_2$CO$_3$ and HCO$_3^-$ through their corresponding dissociation reactions as well as the CO$_2$ hydration reaction.
- The effect of HCO$_3^-$ on cathodic currents is more prominent at pH 6 and elevated CO$_2$ partial pressures that was observed as "double

wave" in cathodic polarization data. That was found to be due to its high concentration and the favorably high surface pH reached at such conditions.
- The rate of the iron dissolution reaction in the transition and pre-passivation ranges is increased significantly with increasing CO$_2$ partial pressures. However, this effect was reduced at higher pH values.
- The effect of non-ideal solutions can be successfully incorporated in the comprehensive mathematical models, based on Pitzer's specific interaction model. The results demonstrate the extent and complexity of the electrochemical response of the system in non-ideal solutions.
- The polarization behavior and the corrosion rates calculated using the present model were found to agree reasonably well with the data obtained experimentally across a broad range of conditions. That was considered as further support for the mechanistic discussions of the present study.

Data availability

The raw/processed data required to reproduce these findings cannot be shared at this time as the data also forms part of an ongoing study.

Appendix A. The equilibrium constant and rate constants of CO$_2$ hydration and H$_2$CO$_3$ dissociation reactions

In the absence of the electrochemical reactions associated with the carbonate species, the magnitude of the limiting current in CO$_2$/H$_2$O system can only be predicted properly if the kinetics and thermodynamics of homogeneous chemical reactions are accurately represented. The equilibrium constant of the CO$_2$ hydration reaction is given a special attention here, due to its significance in CO$_2$ corrosion and the uncertainties surrounding the existing literature data. The CO$_2$ hydration reaction and its equilibrium constant, K_{hyd}, have been discussed in a number of studies over the past few decades [5,58,74–77]. However, this parameter is known with the least certainty amongst all equilibrium constants in the CO$_2$/H$_2$O system, perhaps due to the experimental difficulty of distinguishing H$_2$CO$_3$ from the dissolved CO$_2$. On the other hand, the equilibrium constant of the dissociation reaction in terms of CO$_2$* (Reaction (13)) is known with a good accuracy.

The equilibrium constant of the hydration reaction can be obtained through Equation (17) if K_{Ca} is known. A number of experimental measurements of pK_{Ca} reported in the literature are collected in Table A1, earlier studies on this are reviewed by Kern [58] and are omitted from this table. The reported pK_{Ca} values show a rather significant scattering. In addition to inherent uncertainties of equilibrium constant measurements, the fact that H$_2$CO$_3$ dissociation is strongly affected by the non-ideal solution chemistry can be the source of the observed scattering. The calculations of

Table A1
Reported values of H_2CO_3 dissociation constant (K_{Ca}) at 25 °C.

Reference	pK_{Ca}
Pines et al. (2016) [4]	3.49
Wang et al. (2010) [5]	3.70[a]
Wang et al. (2010) [5]	3.53[b]
Adamczyk et al. (2009) [7]	3.45
Soli and Byrne (2002) [76]	3.42[c]
Wissbrun et al. (1954) [79]	3.76
Roughton (1941) [94]	3.60
This study	3.49

[a] Originally reported values based on unspecified reference of K_{Ca}^*.
[b] Recalculated based of reported K_{hyd} by Wang et al. and K_{Ca}^* from Duan and Li [6].
[c] Authors calculated this value from measured pK_{Ca} = 3.04 at 0.65 m NaCl, using the correction for activities from Harned and Bonner [95].
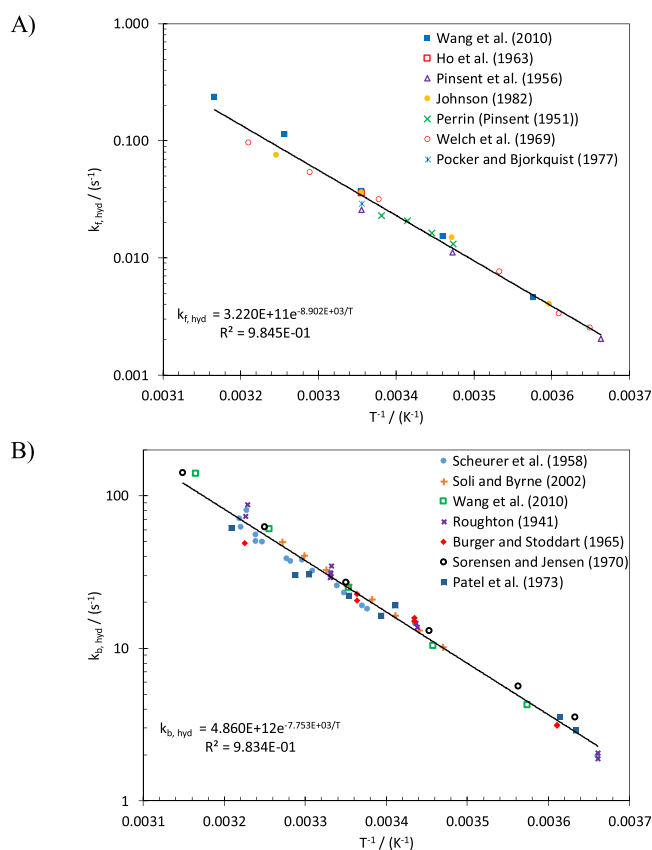

Fig. A1. Experimental values of (A) $k_{f,hyd}$ from Wang et al. [5], Ho and Sturtevant [98], Pinsent et al. [56], Johnson [57], Perrin [99], Welch et al. [100], and Pocker and Bjorkquist [101]. B) $k_{b,hyd}$ from Scheurer et al. [102], Soli and Byrne [76], Wang et al. [5], Roughton [94], Burger and Stoddart [103], Sorensen and Jensen [104], and Patel et al. [105].

Table A2

The Arrhenius parameters for the kinetics rate constants and the equilibrium constant of CO_2 hydration reaction (from 0 to 45 °C).

Parameter	A_0 (s^{-1})	E_a (kJ)
$k_{f,hyd}$ (s^{-1})	3.22×10^{11}	74.011
$k_{b,hyd}$ (s^{-1})	4.86×10^{12}	64.485
K_{hyd}	6.633×10^{-2}	9.526

activity coefficients at 25 °C for 0.1 M and 0.5 M NaCl concentrations result in a factor of 1.4 and 2 difference, respectively (corresponding to 0.15 and 0.3 pK units) between the apparent equilibrium constant and that in infinitely dilute solution. In order to determine the pK_{Ca} values from indirect methods (e.g. spectroscopic pH measurements), a rather extensive water chemistry calculation is required in the data analysis [4,5,76]. Hence, values can only be obtained with sufficient confidence if the non-ideal behavior is meticulously accounted for in data analysis.

If the K_{hyd} is obtained from K_{Ca} values, the above-mentioned uncertainties are carried over into this estimated value. In fact, the value of K_{hyd} = 2.58×10^{-3} that is commonly used in the literature [19,21,42,73,75,78] is based on the pK_{Ca} reported by Wissbrun et al. [79]. That value resides at the higher end of the reported range of equilibrium constants, as shown in Table A1. Other reported pK_{Ca} values would result in significantly different K_{hyd}. For example, the pK_{Ca} = 3.42, reported by Soli and Byrne [76] results in K_{hyd} = 1.15×10^{-3}.

The value of K_{hyd} can also be obtained from the kinetic rate constants of the forward and backward CO_2 hydration reaction based on $K_{hyd} = k_{f,hyd}/k_{bhyd}$. Unlike K_{Ca}, K_{hyd} is not significantly influenced by non-ideal chemistry of the solution. As is apparent from Equation (67), K_{hyd} is a function of the activity of the neutral species, CO_2, H_2CO_3, and H_2O, which are less affected by the non-ideality of the solution. Therefore, one can conclude that the values obtained from $K_{hyd} = k_{f,hyd}/k_{bhyd}$ are more reliable, at least as far as it concerns the effect of non-idealities.

Here, the kinetic rate constants are re-evaluated from a number of experimental data previously reported in the literature, excluding those where a pre-defined K_{Ca} was used in data analysis. As shown Fig. A1 and Fig. B1, the rate constants of the forward and backward partials of hydration reaction and their temperature dependence were obtained based on the Arrhenius law:

$$k = A_0 e^{(-\frac{E_a}{RT})} \tag{66}$$

where, A_0, the pre-exponent parameter, and E_a, the activation energy in Equation (66), for $k_{f,hyd}$, k_{bhyd}, and K_{hyd} are listed in Table A2. These results show that K_{hyd} is a weak function of temperature when comparing the activation energy with those of the forward and backward rate constants. That is in accordance with what is previously reported in the literature. [75,76].

The value of K_{hyd} obtained in the present study (Table A2), alongside with K_{Ca}^* from Duan and Li [6,51] was used to obtain the K_{Ca} at an extended temperature and pressure range. Considering the relatively small effect of non-ideality and temperature on K_{hyd}, the resulting values can be considered to reasonably represent the true equilibrium constant of H_2CO_3 dissociation. This procedure results in K_{Ca} = 3.49 at 25 °C, which is in agreement with the values obtained independently in the more recent studies [4,5,7].

Appendix B. Pitzer parameters of CO_2–H_2O–NaCl system

The Pitzer parameters for the interaction of the species in $H_2O - CO_2$-NaCl system used in the present study are shown in Table B1. The second virial coefficients $\beta^{(0)}$ and $\beta^{(1)}$ and the single electrolyte third virial coefficient C^{φ} of H^+–Cl^-, Na^+–Cl^-, $Na^+ - OH$- are from studies by Holmes et al. [80], Moller [81], Pabalan and Pitzer [82], respectively. The interaction of Na^+ with carbonate (CO_3^{2-}) and bicarbonate ions (HCO_3^-) have been studied by a number of researchers showing a reasonable agreement when the whole set of parameters are used in the model. The results reported by Polya et al. [83], were used in the present study as they cover a wide pressure (up to 70 bar) and temperature ranges (298–523 K). The second virial Pitzer parameters (θ), describing the interaction of the ions with the same charge, are based on the study by Christov and Moller [84].

The ion-neutral species Pitzer interaction parameter, associated with dissolved CO_2 and Na^+ and Cl^-, are based on the study of He et al. [85]. The interaction of CO_2 with bicarbonate and carbonate ions can also be significant at high CO_2 partial pressures and also at near neutral/alkaline solutions where the concentrations of these species are large. In addition to affecting the solubility of CO_2, through its activity coefficient, the major influence of this parameter is on the activity coefficient of bicarbonate and carbonate ions.

As it can be seen in Eq. (21), the term $m_n\lambda_{nx}$ depends on the concentration of dissolved CO_2, which can be large at high CO_2 partial pressures (~0.5 m at 20 bar). However, the reported values for this parameter in a studies by Li and Duan [51] and Wong et al. [86] are widely different, and result in significant inconsistencies in speciation calculations. Hence, they are not included in the present model. This can be due to a lack of sufficient experimental data obtained across a reasonably large range of parameters (T and pCO_2), used for obtaining these parameters. The Pitzer parameters for H_2CO_3 are not available in the literature, perhaps due to the experimental difficulties in its distinction from dissolved CO_2. Due to the lack of a better understanding, the Pitzer parameters reported for CO_2 were also used to determine the activity coefficient of H_2CO_3.

Table B1
Pitzer parameters of $H_2O - CO_2 - NaCl$ system (all values are rounded to four significant digits).

Parameter	c_1	c_2	c_3	c_4	c_5	c_6	Ref.
$\beta^{(0)}_{H^+,Cl^-}$ *	1.7690×10^{-1}	-9.1400×10^{-2}	0.0	-4.0340×10^{-4}	6.2000×10^{-6}	—	[80]
$\beta^{(1)}_{H^+,Cl^-}$ *	2.9730×10^{-1}	1.6147×10^{1}	-1.7631×10^{-2}	0.0000	7.2000×10^{-5}	—	[80]
$C^{\phi}_{H^+,Cl^-}$ *	7.2400×10^{-4}	0.0	0.0	-6.0720×10^{-5}	0.0	—	[80]
$\beta^{(0)}_{Na^+,Cl^-}$ **	1.4378×10^{1}	5.6077×10^{-3}	-4.2219×10^{2}	-2.5123	0.0	-2.6172×10^{-6}	[81]
$\beta^{(1)}_{Na^+,Cl^-}$ **	-4.8306×10^{-1}	1.4068×10^{-3}	1.1931×10^{2}	0.0	0.0	0.0	[81]
$C^{\phi}_{Na^+,Cl^-}$ **	-1.0059×10^{-1}	-1.8053×10^{-5}	8.6119	1.2488×10^{-2}	0.0	3.4117×10^{-8}	[81]
$\beta^{(0)}_{Na^+,OH^-}$ †	2.7682×10^{2}	-2.8142×10^{-3}	-7.3755×10^{3}	3.7013×10^{-1}	-4.9360×10^{1}	1.0945×10^{-1}	[82]
$\beta^{(1)}_{Na^+,OH^-}$ †	4.6287×10^{2}	0.0	-1.0294×10^{4}	0.0000	-8.5961×10^{1}	2.3906×10^{-1}	[82]
$C^{\phi}_{Na^+,OH^-}$ †	-1.6687×10^{1}	4.0535×10^{-4}	4.5365×10^{2}	-5.1714×10^{-2}	2.9681	-6.5162×10^{-3}	[82]
$\beta^{(0)}_{Na^+,HCO_3^-}$ ‡	6.6100×10^{-2}	0.0	0.0	0.0	0.0	3.7595×10^{-8}	
$\beta^{(1)}_{Na^+,HCO_3^-}$ ‡	-4.1160	6.3090×10^{-3}	9.2400×10^{2}	-5.2020×10^{1}	-8.0260×10^{1}	0.0	
$C^{\phi}_{Na^+,HCO_3^-}$ ‡	0.0	0.0	0.0	0.0	0.0	0.0	
$\beta^{(0)}_{Na^+,CO_3^{2-}}$ ‡	5.1530×10^{-1}	-5.9910×10^{-4}	0.0	-2.5810×10^{1}	-2.6590	0.0	
$\beta^{(1)}_{Na^+,CO_3^{2-}}$ ‡	2.0440	-4.3030×10^{-3}	0.0	-2.5450×10^{1}	3.6180×10^{2}	0.0	
$C^{\phi}_{Na^+,CO_3^{2-}}$ ‡	-9.1400×10^{-2}	0.0	0.0	6.4820	8.0480	0.0	
θ_{Na^+,H^+} #	4.8136×10^{-2}	0.0	0.0	-4.0543	—	—	
θ_{Cl^-,OH^-} #	1.1049×10^{-1}	0.0	0.0	-4.9361×10^{1}	—	—	
θ_{Cl^-,HCO_3^-} #	3.5900×10^{-2}	—	—	—	—	—	
$\theta_{Cl^-,CO_3^{2-}}$ #	-5.3000×10^{-2}	—	—	—	—	—	
$\theta_{HCO_3^-,CO_3^{2-}}$ #	-4.0000×10^{-2}	—	—	—	—	—	
$\theta_{CO_3^{2-},OH^-}$ #	1.0000×10^{-1}	—	—	—	—	—	
λ_{CO_2,Na^+} ◊	-5.4964×10^{3}	-3.3266	1.7532×10^{-3}	1.0940×10^{5}	1.0470×10^{3}	—	
λ_{CO_2,Cl^-} ◊	1.6599×10^{3}	9.9643×10^{-5}	5.2122×10^{-4}	3.3160×10^{4}	3.1583×10^{2}	—	
λ_{CO_2,CO_2} ◊◊	-8.6035×10^{-1}	3.2971×10^{-3}	6.3093×10^{1}	-4.0990×10^{-6}	1.5295×10^{1}	6.5066×10^{-3}	

Parameter	c_7	c_8	c_9	c_{10}	c_{11}	c_{12}
$\beta^{(0)}_{H^+,Cl^-}$ *	—	—	—	—	—	—
$\beta^{(1)}_{H^+,Cl^-}$ *	—	—	—	—	—	—
$C^{\phi}_{H^+,Cl^-}$ *	—	—	—	—	—	—
$\beta^{(0)}_{Na^+,Cl^-}$ **	4.4385	-1.7050	—	—	—	—
$\beta^{(1)}_{Na^+,Cl^-}$ **	0.0	-4.2343	—	—	—	—
$C^{\phi}_{Na^+,Cl^-}$ **	6.8304×10^{-2}	2.9392×10^{-1}	—	—	—	—
$\beta^{(0)}_{Na^+,OH^-}$ †	7.1789×10^{-6}	-4.0219×10^{-5}	-5.8847×10^{-9}	1.1931×10^{1}	2.4825	-4.8217×10^{-3}
$\beta^{(1)}_{Na^+,OH^-}$ †	0.0	-1.0796×10^{-4}	0.0	0.0	0.0	0.0
$C^{\phi}_{Na^+,OH^-}$ †	-1.0553×10^{-6}	2.3766×10^{-6}	8.9893×10^{-10}	-6.8924×10^{-1}	-8.1156×10^{-2}	0.0

Table B1 (continued)

Parameter	c_7	c_8	c_9	c_{10}	c_{11}	c_{12}	Ref.
$\beta^{(0)}_{Na^+,HCO_3^-}$ ‡	0.0	0.0	–	–	–	–	[83]
$\beta^{(1)}_{Na^+,HCO_3^-}$ ‡	1.6340×10^{-4}	-1.3900×10^{-7}	–	–	–	–	[83]
$C^{\phi}_{Na^+,HCO_3^-}$ ‡	0.0	0.0	–	–	–	–	[83]
$\beta^{(0)}_{Na^+,CO_3^{2-}}$ ‡	8.7500×10^{-5}	-2.6600×10^{-8}	–	–	–	–	[83]
$\beta^{(1)}_{Na^+,CO_3^{2-}}$ ‡	0.0	0.0	–	–	–	–	[83]
$C^{\phi}_{Na^+,CO_3^{2-}}$ ‡	-2.8900×10^{-5}	0.0	–	–	–	–	[83]
θ_{Na^+,H^+} #	–	–	–	–	–	–	[84]
θ_{Cl^-,OH^-} #	–	–	–	–	–	–	[84]
θ_{Cl^-,HCO_3^-} #	–	–	–	–	–	–	[96]
$\theta_{Cl^-,CO_3^{2-}}$ #	–	–	–	–	–	–	[96]
$\theta_{HCO_3^-,CO_3^{2-}}$ #	–	–	–	–	–	–	[97]
$\theta_{CO_3^{2-},OH^-}$ #	–	–	–	–	–	–	[97]
λ_{CO_2,Na^+} ◊	–	–	–	–	–	–	[85]
λ_{CO_2,Cl^-} ◊	–	–	–	–	–	–	[85]
λ_{CO_2,CO_2} ◊◊	-9.6380×10^{-4}	-3.2382×10^{-1}	1.5991×10^{-2}	0.0000	1.8867×10^{-5}	–	[51]

* Parameter $= c_1 + c_2 \ln\left(\frac{\rho_T}{\rho_{298.15}}\right) + c_3 (\rho_T - \rho_{298.15}) + c_4 (T - 298.15) + c_5 (P - 1)$, where ρ_T, density in kg m^{-3} at temperature T, and pressure P in bar.

** Parameter $= c_1 + c_2 T + \frac{c_3}{T} + c_4 \ln(T) + \frac{c_5}{T-263} + c_6 T^2 + \frac{c_7}{680-T} + c_7/(T-227)$

† Parameter $= c_1 + c_2 P + \frac{c_3 + c_4 P}{T} + c_5 \ln(T) + (c_6 + c_7 P)T + \frac{c_{10}}{T-227} + \frac{(c_{11}+c_{12}P)}{647-T}$

‡ Parameter $= c_1 + c_2 T + \frac{c_3}{T} + \frac{c_4}{T-210} + \frac{c_5}{647-T} + c_6 \frac{(T-443)^3}{3} + c_7 (P-1) + \frac{c_8(P-1)^2}{2}$

\# Parameter $= c_1 + c_2 T + c_3 T^2 + c_4 T^3$

◊ Parameter $= c_1 + c_2 T + c_3 T^2 + \frac{c_4}{T} + c_5 \ln(T)$

◊◊ Parameter $= c_1 + c_2 T + \frac{c_3}{T} + c_4 T^2 + \frac{c_5}{630-T} + c_6 P + c_7 P\ln(T) + \frac{c_8 P}{T} + \frac{c_9 P}{630-T} + \frac{c_{10}P^2}{(630-T)2} + c_{11} T\ln(P)$

References

[1] R.E. Zeebe, D.A. Wolf-Gladrow, H. Jansen, On the time required to establish chemical and isotopic equilibrium in the carbon dioxide system in seawater, Mar. Chem. 65 (1999) 135–153, https://doi.org/10.1016/S0304-4203(98)00092-9.

[2] R.E. Zeebe, D. Wolf-Gladrow, CO_2 in Seawater: Equilibrium, Kinetics, Isotopes, Elsevier, 2001, https://doi.org/10.1016/S0422-9894(01)80001-5.

[3] K.G. Schulz, U. Riebesell, B. Rost, S. Thoms, R.E. Zeebe, Determination of the rate constants for the carbon dioxide to bicarbonate inter-conversion in pH-buffered seawater systems, Mar. Chem. 100 (2006) 53–65, https://doi.org/10.1016/j.marchem.2005.11.001.

[4] D. Pines, J. Ditkovich, T. Mukra, Y. Miller, P.M. Kiefer, S. Daschakraborty, J.T. Hynes, E. Pines, How acidic is carbonic acid? J. Phys. Chem. B 120 (2016) 2440–2451, https://doi.org/10.1021/acs.jpcb.5b12428.

[5] X. Wang, W. Conway, R. Burns, N. McCann, M. Maeder, Comprehensive study of the hydration and dehydration reactions of carbon dioxide in aqueous solution, J. Phys. Chem. A 114 (2010) 1734–1740, https://doi.org/10.1021/jp909019u.

[6] Z. Duan, D. Li, Coupled phase and aqueous species equilibrium of the $H_2O–CO_2–NaCl–CaCO_3$ system from 0 to 250°C, 1 to 1000 bar with NaCl concentrations up to saturation of halite, Geochim. Cosmochim. Acta 72 (2008) 5128–5145, https://doi.org/10.1016/j.gca.2008.07.025.

[7] A. Adamczyk, M. Prémont-Schwarz, D. Pines, E. Pines, E. Nibbering, Real-time observation of carbonic acid formation in aqueous solution, Science 326 (2009) 1690–1694, https://doi.org/10.1126/science.1180060.

[8] Z. Duan, R. Sun, An improved model calculating CO_2 solubility in pure water and aqueous NaCl solutions from 273 to 533 K and from 0 to 2000 bar, Chem. Geol. 193 (2003) 257–271, https://doi.org/10.s0009-2541(02)00263-2.

[9] A. Kahyarian, M. Achour, S. Nesic, Mathematical modeling of uniform co_2 corrosion, in: A.M. El-Sherik (Ed.), Trends Oil Gas Corros. Res. Technol. Prod. Transm, Elsevier, 2017, pp. 805–849, , https://doi.org/10.1016/B978-0-08-101105-8.00034-6.

[10] A. Kahyarian, M. Achour, S. Nesic, CO_2 corrosion of mild steel, in: A.M. El-Sherik (Ed.), Trends Oil Gas Corros. Res. Technol. Prod. Transm. Elsevier, 2017, pp. 149–190, , https://doi.org/10.1016/B978-0-08-101105-8.00007-3.

[11] A. Kahyarian, M. Singer, S. Nesic, Modeling of uniform CO2 corrosion of mild steel in gas transportation systems: a review, J. Nat. Gas Sci. Eng. 29 (2016) 530–549, https://doi.org/10.1016/j.jngse.2015.12.052.

[12] C. de Waard, D.E. Milliams, Prediction of carbonic acid corrosion in natural gas pipelines, Intern. Extern. Prot. Pipes (1975) pp. F1-1-F1-8.

[13] C. de Waard, D.E. Milliams, Carbonic acid corrosion of steel, Corrosion. 31 (1975) 177–181, https://doi.org/10.5006/0010-9312-31.5.177.

[14] G. Schmitt, B. Rothmann, Studies on the Corrosion Mechanism of Unalloyed Steel in Oxygen-Free Carbon Dioxide Solutions. Part I. Kinetics of the Liberation of Hydrogen Vol. 28 Werkstoffe Und Korrosion., 1977, p. 816.

[15] L.G.S. Gray, B.G. Anderson, M.J. Danysh, P.R. Tremaine, Mechanisms of carbon steel corrosion in brines containing dissolved carbon dioxide At pH 4, Corrosion (1989) 464 p. Paper No..

[16] L.G.S. Gray, B.G. Anderson, M.J. Danysh, P.R. Tremaine, Effect of pH and temperature on the mechanism of carbon steel corrosion by aqueous carbon dioxide, Corrosion (1990) 40 p. Paper No..

[17] S. Turgoose, R.A. Cottis, K. Lawson, Modeling of electrode processes and surface chemistry in carbon dioxide containing solutions, Comput. Model. Corros. ASTM STP 1154 (1992) 67–81.

[18] B.F.M. Pots, Mechanistic models for the prediction of CO_2 corrosion rates under multi-phase flow conditions, Corrosion (1995) 137 Paper No.

[19] M. Nordsveen, S. Nešić, R. Nyborg, A. Stangeland, A mechanistic model for carbon dioxide corrosion of mild steel in the presence of protective iron carbonate films - part 1: theory and verification, Corrosion. 59 (2003) 443–456, https://doi.org/10.5006/1.3277592.

[20] S. Nešić, M. Nordsveen, R. Nyborg, A. Stangeland, A mechanistic model for CO_2 corrosion with protective iron carbonate films, Corrosion (2001) 040 Paper No..

[21] Y. Zheng, J. Ning, B. Brown, S. Nesic, Electrochemical model of mild steel corrosion in a mixed H_2S/CO_2 aqueous environment, Corrosion 71 (2014) (2014) 316–325.

[22] J. Han, J. Zhang, J.W. Carey, Effect of bicarbonate on corrosion of carbon steel in CO_2 saturated brines, Int. J. Greenh. Gas Control. 5 (2011) 1680–1683, https://doi.org/10.1016/j.ijggc.2011.08.003.

[23] J. Han, J.W. Carey, J. Zhang, Effect of sodium chloride on corrosion of mild steel in CO2-saturated brines, J. Appl. Electrochem. 41 (2011) 741–749, https://doi.org/10.1007/s10800-011-0290-3.

[24] S. Nešić, J. Postlethwaite, S. Olsen, An electrochemical model for prediction of corrosion of mild steel in aqueous carbon dioxide solutions, Corrosion 52 (1996) 280–294.

[25] T. Tran, B. Brown, S. Nešic, B. Tribollet, Investigation of the electrochemical mechanisms for acetic acid corrosion of mild steel, Corrosion 70 (2014) 223–229.

[26] J. Amri, E. Gulbrandsen, P.R. Nogueira, Effect of acetic acid on propagation and stifling of localized attacks in CO_2 corrosion of carbon steel, Corrosion (2009) 284 p. Paper No..

[27] A. Kahyarian, A. Schumaker, B. Brown, S. Nesic, Acidic corrosion of mild steel in the presence of acetic acid: mechanism and prediction, Electrochim. Acta 258 (2017) 639–652, https://doi.org/10.1016/j.electacta.2017.11.109.

[28] A. Kahyarian, B. Brown, S. Neší, Mechanism of cathodic reactions in acetic acid corrosion of iron and mild steel, Corrosion 72 (2016) 1539–1546, https://doi.org/10.5006/2177.

[29] K.S. George, S. Nešić, Investigation of carbon dioxide corrosion of mild steel in the

[30] presence of acetic acid-part 1: basic mechanisms, Corrosion (2007) 178–186, https://doi.org/10.5006/1.3278342.

[30] Z. Jia, X. Li, C. Du, Z. Liu, J. Gao, Effect of acetic acid on CO_2 corrosion of 3Cr low-alloy steel, Mater. Chem. Phys. 132 (2012) 258–263, https://doi.org/10.1016/j.matchemphys.2011.08.034.

[31] B.R. Linter, G.T. Burstein, Reactions of pipeline steels in carbon dioxide solutions, Corros. Sci. 41 (1999) 117–139, https://doi.org/10.1016/S0010-938X(98)00104-8.

[32] E. Remita, B. Tribollet, E. Sutter, V. Vivier, F. Ropital, J. Kittel, Hydrogen evolution in aqueous solutions containing dissolved CO_2: quantitative contribution of the buffering effect, Corros. Sci. 50 (2008) 1433–1440, https://doi.org/10.1016/j.corsci.2007.12.007.

[33] T. Tran, B. Brown, S. Nešić, Corrosion of mild steel in an aqueous CO_2 environment – basic electrochemical mechanisms revisited, Corrosion (2015) 671 p. Paper no..

[34] A. Kahyarian, B. Brown, S. Nesic, S. Ne, Technical note: electrochemistry of CO_2 corrosion of mild steel : effect of CO_2 on cathodic currents, Corrosion 74 (2018) 851–859, https://doi.org/10.5006/2792.

[35] A. Kahyarian, S. Nesic, A new narrative for CO_2 corrosion of mild steel, J. Electrochem. Soc. 166 (2019) C3048–C3063, https://doi.org/10.1149/2.0071911jes.

[36] A. Kahyarian, B. Brown, S. Nešić, Technical note: electrochemistry of CO_2 corrosion of mild steel: effect of CO_2 on cathodic currents, Corrosion. 74 (2018) 851–859, https://doi.org/10.5006/2792.

[37] A. Kahyarian, B. Brown, S. Nesic, Mechanism of CO_2 corrosion of mild steel: a new narrative, in: NACE - Int, Corros. Conf. Ser. (2018) 1–16.

[38] A. Kahyarian, B. Brown, S. Nesic, Electrochemistry of CO_2 corrosion of mild steel: effect of CO_2 on iron dissolution reaction, Corros. Sci. 129 (2017) 146–151, https://doi.org/10.1016/j.corsci.2017.10.005.

[39] F.V.V. de Sousa, N.A. Leite, B. Tribollet, O.E. Barcia, O.R. Mattos, Model for hydrogen evolution reaction in aqueous solutions containing dissolved CO_2 in high pressures, J. Electrochem. Soc. 166 (2019) C479–C484, https://doi.org/10.1149/2.0421914jes.

[40] aria kahyarian, B. Brown, S. Nesic, The unified mechanism of corrosion in aqueous weak acids solutions: a review of the recent developments in mechanistic understandings of mild steel corrosion in the presence of carboxylic acids, carbon dioxide, and hydrogen sulfide, Corrosion (2020), https://doi.org/10.5006/3474.

[41] S. Nešić, Carbon dioxide corrosion of mild steel, in: Uhlig's Corros. Handb. third ed., (2011), pp. 229–245, https://doi.org/10.1002/9780470872864.ch19.

[42] S. Nešić, W. Sun, Corrosion in acid gas solutions, Shreir's Corros. (2010) 1270–1298.

[43] S. Nešić, A. Kahyarian, Y.S. Choi, Implementation of a comprehensive mechanistic prediction model of mild steel corrosion in multiphase oil and gas pipelines, Corrosion. 75 (2019) 274–291, https://doi.org/10.5006/3093.

[44] S. Nesic, M. Nordsveen, R. Nyborg, A. Stangeland, A mechanistic model for CO2corrosion with protective iron carbonate films, NACE - Int. Corros. Conf. Ser. 2001 (March) (2001).

[45] F.M. Song, D.W. Kirk, J.W. Graydon, D.E. Cormack, Predicting carbon dioxide corrosion of bare steel under an aqueous boundary layer, Corrosion. 60 (2004) 736–748, https://doi.org/10.5006/1.3287866.

[46] F.M. Song, A comprehensive model for predicting CO_2 corrosion rate in oil and gas production and transportation systems, Electrochim. Acta 55 (2010) 689–700, https://doi.org/10.1016/j.electacta.2009.07.087.

[47] I.R. Krichevsky, J.S. Kasarnovsky, Thermodynamical calculations of solubilities of nitrogen and hydrogen in water at high pressures, J. Am. Chem. Soc. 57 (1935) 2168–2171, https://doi.org/10.1021/ja01314a036.

[48] J.J. Carroll, A.E. Mather, The system carbon dioxide-water and the Krichevsky-Kasarnovsky equation, J. Solution Chem. 21 (1992) 607–621, https://doi.org/10.1007/BF00650756.

[49] V. Majer, J. Sedlbauer, G. Bergin, Henry's law constant and related coefficients for aqueous hydrocarbons, CO2and H2S over a wide range of temperature and pressure, Fluid Phase Equilib. 272 (2008) 65–74, https://doi.org/10.1016/j.fluid.2008.07.013.

[50] J. Garcia, Density of aqueous solutions of CO (2001).

[51] D. Li, Z. Duan, The speciation equilibrium coupling with phase equilibrium in the $H_2O–CO_2–NaCl$ system from 0 to 250 °C, from 0 to 1000 bar, and from 0 to 5 molality of NaCl, Chem. Geol. 244 (2007) 730–751, https://doi.org/10.1016/j.chemgeo.2007.07.023.

[52] Z. Duan, R. Sun, C. Zhu, I.-M. Chou, An improved model for the calculation of CO2 solubility in aqueous solutions containing Na +, K +, Ca2 +, Mg2 +, Cl −, and SO4 −, Mar. Chem. 98 (2006) 131–139, https://doi.org/10.1016/j.marchem.2005.09.001.

[53] K.S. Pitzer, Thermodynamics of electrolytes: V. Effects of higher order electrostatic terms, J. Solution Chem. 4 (1975) 249–265.

[54] M. Eigen, Proton transfer, acid-base catalysis, and enzymatic hydrolysis, angew, Chem. Int. Ed. Engl. 3 (1964) 1–19.

[55] F.H. Stillinger, Proton transfer reactions and kinetics in water, Theor. Chem. Adv. 3 (1978) 177–234.

[56] B.R.W. Pinsent, L. Pearson, F.J.W. Roughton, The kinetics of combination of carbon dioxide with hydroxide ions, Trans. Faraday Soc. 52 (1956) 1512, https://doi.org/10.1039/tf9565201512.

[57] K.S. Johnson, Carbon dioxide hydration kinetics in seawater and dehydration, Limnol. Oceanogr. 27 (1982) 849–855.

[58] D.M. Kern, The hydration of carbon dioxide, J. Chem. Educ. 37 (1960) 14–23, https://doi.org/10.1021/ed037p14.

[59] J. Newman, K.E. Thomas-Alyea, Electrochemical Systems, 3rd ed., Wiley-

interscience, 2004.

[60] J.T. Davies, S.T. Ting, Mass transfer into turbulent jets, Chem. Eng. Sci. 22 (1967) 1539–1548, https://doi.org/10.1016/0009-2509(67)80192-1.

[61] S. Aravinth, Prediction of heat and mass transfer for fully developed turbulent fluid flow through tubes, Int. J. Heat Mass Transf. 43 (2000) 1399–1408, https://doi.org/10.1016/S0017-9310(99)00218-5.

[62] P.K. Swamee, A.K. Jain, Explicit equations for pipe-flow problems, J. Hydraul. Div. 102 (1976) 657–664.

[63] C.F. Colebrook, C.M. White, Experiments with fluid friction in roughened pipes, Proc. R. Soc. A Math. Phys. Eng. Sci. 161 (1937) 367–381, https://doi.org/10.1098/rspa.1937.0150.

[64] J. Newman, Numerical solution of coupled, ordinary differential equations, Ind. Eng. Chem. Fundam. 7 (1968) 514–517.

[65] A. Kahyarian, B. Brown, S. Nesic, Mechanism of the hydrogen evolution reaction in mildly acidic environments on gold, J. Electrochem. Soc. 164 (2017) H365–H374, https://doi.org/10.1149/2.1061706jes.

[66] B. Meyssami, M.O. Balaban, A.A. Teixeira, Prediction of pH in model systems pressurized with carbon dioxide, Biotechnol. Prog. 8 (1992) 149–154, https://doi.org/10.1021/bp00014a009.

[67] J.-L. Crolet, M.R. Bonis, pH measurements in aqueous CO2 solutions under high pressure and temperature, Corrosion. 39 (1983) 39–45.

[68] A.A. El Miligy, D. Geana, W.J. Lorenz, A theoretical treatment of the kinetics of iron dissolution and passivation, Electrochim. Acta 20 (1975) 273–281, https://doi.org/10.1016/0013-4686(75)90005-5.

[69] J. Kittel, F. Ropital, F. Grosjean, E.M.M. Sutter, B. Tribollet, Corrosion mechanisms in aqueous solutions containing dissolved H2S. Part 1: characterisation of H2S reduction on a 316L rotating disc electrode, Corros. Sci. 66 (2013) 324–329, https://doi.org/10.1016/j.corsci.2012.09.036.

[70] B. Tribollet, J. Kittel, A. Meroufel, F. Ropital, F. Grosjean, E.M.M. Sutter, Corrosion mechanisms in aqueous solutions containing dissolved H2S. Part 2: model of the cathodic reactions on a 316L stainless steel rotating disc electrode, Electrochim. Acta 124 (2014) 46–51, https://doi.org/10.1016/j.corsci.2012.09.036.

[71] Y. Zheng, B. Brown, S. Nešic, Electrochemical study and modeling of H2S corrosion of mild steel, Corrosion. 70 (2014) 351–365.

[72] Y. Xiang, C. Li, Z. Long, C. Guan, W. Wang, W. Hesitao, Electrochemical behavior of valve steel in a CO2/sulfurous acid solution, Electrochim. Acta 258 (2017) 909–916, https://doi.org/10.1016/j.electacta.2017.11.141.

[73] J. Han, J.W. Carey, J. Zhang, A coupled electrochemical-geochemical model of corrosion for mild steel in high-pressure CO2-saline environments, Int. J. Greenh. Gas Control. 5 (2011) 777–787, https://doi.org/10.1016/j.ijggc.2011.02.005.

[74] T.H.M.Lal C. Garg, The rates of hydration of carbon dioxide and dehydration of carbonic acid at 37°, Biochim. Biophys. Acta 261 (1971) 70–76.

[75] D.A. Palmer, R. Van Eldik, The chemistry of metal carbonat and carbon dioxide complexes, Chem. Rev. 83 (1983) 651–731, https://doi.org/10.1021/cr00058a004.

[76] A.L. Soli, R.H. Byrne, CO2 system hydration and dehydration kinetics and the equilibrium CO2/H2CO3 ratio in aqueous NaCl solution, Mar. Chem. 78 (2002) 65–73, https://doi.org/10.1016/S0304-4203(02)00010-5.

[77] W. Stumm, J.J. Morgan, Aquatic Chemistry: Chemical Equilibria and Rates in Natural Waters, 3rd editio, Wiley-Interscience, 1995.

[78] R. Alberty, Standard transformed formation properties of carbon dioxide in aqueous solutions at specified pH, J. Phys. Chem. 99 (1995) 11028–11034, https://doi.org/10.1021/j100027a051.

[79] K.F. Wissbrun, D.M. French, A. Patterson Jr., The true ionization constant of carbonic acid in aqueous solution from 5-degrees to 45-degrees, J. Phys. Chem. 58 (1954) 693–695.

[80] H.F. Holmes, R.H. Busey, J.M. Simonson, R.E. Mesmer, D.G. Archer, R.H. Wood, The enthalpy of dilution of HCl(aq) to 648 K and 40 MPa thermodynamic properties, J. Chem. Thermodyn. 19 (1987) 863–890, https://doi.org/10.1016/0021-9614(87)90033-4.

[81] N. Moller, The prediction of mineral solubilities in natural waters: a chemical equilibrium model for the Na-Ca-C1-S04-H20 system, to high temperature and concentration, Geochim. Cosmochim. Acta 52 (1988) 821–837.

[82] R.T. Pabalan, K.S. Pitzer, Thermodynamics of NaOH (aq) in hydrothermal solutions, Geochim. Cosmochim. Acta 51 (1987) 829–837.

[83] D.A. Polya, E.M. Woolley, J.M. Simonson, R.E. Mesmer, The enthalpy of dilution and thermodynamics of Na2CO3(aq) and NaHCO3(aq) from T = 298 K to T = 523.15 K and pressure of 40 MPa, J. Chem. Thermodyn. 33 (2001) 205–243, https://doi.org/10.1006/jcht.2001.0754.

[84] C. Christov, N. Moller, Chemical equilibrium model of solution behavior and solubility in the H-Na-K-OH-Cl-HSO4-SO4-H2O system to high concentration and temperature, Geochim. Cosmochim. Acta 68 (2004) 1309–1331, https://doi.org/10.1016/j.gca.2003.08.017.

[85] S. He, J.W. Morse, The carbonic acid system and calcite solubility in aqueous Na-K-Ca-Mg-Cl-SO4 solutions from 0 to 90°C, Geochim. Cosmochim. Acta 57 (1993) 3533–3554.

[86] C.S. Wong, P.Y. Tishchenko, W.K. Johnson, Effects of high CO2 molality on the carbon dioxide equilibrium of seawater, J. Chem. Eng. Data 50 (2005) 822–831, https://doi.org/10.1021/je049717i.

[87] W.L. Marshall, E.U. Franck, Ion product of water substance, 0-1000 °C, 1-10,000 bars New International Formulation and its background, J. Phys. Chem. Ref. Data 10 (1983) 295–304, https://doi.org/10.1063/1.555643.

[88] J.R. Cooper, Revised Release on the IAPWS Industrial Formulation 1997 for the Thermodynamic Properties of Water and Steam, (2012).

[89] W.C. Natzle, C.B. Moore, Recombination of H+ and OH- in pure liquid water, J. Phys. Chem. 89 (1985) 2605–2612, https://doi.org/10.1017/CBO9781107415324.004.

[90] E.L. Cussler, Diffusion: Mass Transfer in Fluid Systems, third edit, Cambridge University Press, 2007.

[91] W.M. Haynes, CRC Handbook of Chemistry and Physics, 84th ed., CRC Press LLC, 2004.

[92] L. Korson, W. Drost-Hansen, F.J. Millero, Viscosity of water at various temperatures, J. Phys. Chem. 73 (1969) 34–39, https://doi.org/10.1021/j100721a006.

[93] C.L. Yaws, The Yaws Handbook of Vapor Pressure : Antoine Coefficients, (2020) n.d..

[94] F.J.W. Roughton, The kinetics and rapid thermochemistry of carbonic acid, J. Am. Chem. Soc. 63 (1941) 2930–2934, https://doi.org/10.1021/ja01856a018.

[95] H.S. Harned, F.T. Bonner, The first ionization of carbonic acid in aqueous solutions of sodium chloride, J. Am. Chem. Soc. 67 (1945) 1026–1031, https://doi.org/10.1021/ja01222a037.

[96] J.C. Peiper, K.S. Pitzer, Thermodynamics solutions including sodium carbonate, chloride of aqueous carbonate mixtures of bicarbonate, and chloride, J. Chem. Thermodyn. 14 (1982) 613–638.

[97] C.E. Harvie, N. Moeller, J.H. Weare, The prediction of mineral solubilities in natural waters: the Na-K-Mg-Ca-H-CI-SO4-OH-HCO3-CO3-CO2-H2O system to high ionic strengths at 25 C, Geochim. Cosmochim. Acta 48 (1984) 723.

[98] C. Ho, J.M. Sturtevant, The kinetics of the hydration of carbon dioxide at 25ˆ\circC, J. Biol. Chem. 238 (1963) 3499–3501.

[99] B.R.W. Pinsent, F.J.W. Roughton, The kinetics of combination of carbon dioxide with water and Hydroxide Ions, Trans. Faraday Soc. 47 (1951) 263–269.

[100] M.J. Welch, J.F. Lifton, J.A. Seck, Tracer studies with radioactive oxygen-15. Exchange between carbon dioxide and water, J. Phys. Chem. 73 (1969) 3351–3356, https://doi.org/10.1021/j100844a033.

[101] Y. Pocker, D.W. Bjorkquist, Stopped-flow studies of carbon dioxide hydration and bicarbonate dehydration in H2O and D2O. acid-base and metal ion catalysis, J. Am. Chem. Soc. 99 (1977) 6537–6543, https://doi.org/10.1021/ja00462a012.

[102] P.G. Scheurer, R.M. Brownell, J.E. Luvalle, Kinetics of the carbonic acid dehydration, J. Phys. Chem. 62 (1958) 809–812, https://doi.org/10.1021/j150565a009.

[103] R.L. Berger, L.C. Stoddart, Combined calorimeter and spectrophotometer for observing biological reactions, Rev. Sci. Instrum. 36 (1965) 78.

[104] P.E. Sorensen, A. Jensen, The carbonic acid dehydration and its activation energy, Acta Chem. Scand. 24 (1970) 1483–1485.

[105] R.C. Patel, R.J. Boe, G. Atkinson, The CO2-water system. I. Study of the slower hydration-dehydration step, J. Solution Chem. 2 (1973) 357–372, https://doi.org/10.1007/BF00713250.